CRYSTAL GROWTH & DESIGN

pubs.acs.org/crystal

Article

Rose-like NiFe-LDH/MoS_2 Electrocatalysts Achieve 1000 mA cm^{-2} OER with Enhanced Charge Transfer and Seawater Stability

Xin Li,[#] Yue Qin,[#] Bo-yang Zhang, Bo-yao Zhang, Rong-da Zhao,* Jia Li, Depeng Zhao,* and Li-hua Miao*

Cite This: https://doi.org/10.1021/acs.cgd.5c01006

Read Online

ACCESS | Metrics & More | Article Recommendations | Supporting Information

ABSTRACT: Developing highly active electrocatalysts for the oxygen evolution reaction (OER) at large current densities is of paramount importance for water electrolysis. Herein, in situ growth of rose-like NiFe-LDH/MoS_2 heterostructures on nickel foam is prepared through a one-step hydrothermal process, which exhibits outstanding electrocatalytic activity. NiFe-LDH/MoS_2 catalyst drives an industrial-grade current density of 1000 mA cm^{-2} at a low overpotential of only 376 mV in 1.0 M KOH, with a small Tafel slope of 37.34 mV dec^{-1}. When assembled into an electrolyzer for overall water splitting, it reaches 100 mA cm^{-2} at just 1.9 V. Moreover, the catalyst maintains good activity and prolonged stability in alkaline seawater. Density Functional Theory (DFT) calculations confirm that a strong electronic interaction and charge redistribution between NiFe-LDH and MoS_2 optimize the electronic structure, boosting both electrical conductivity and catalytic performance. This work offers a viable new strategy for designing efficient and durable OER catalysts for both freshwater and seawater electrolysis.

1. INTRODUCTION

With the escalating global energy crisis and environmental pollution, the development of clean and renewable alternative energy has become an urgent imperative. Hydrogen energy, by virtue of its advantages including zero carbon emissions, high energy density, and sustainability, is considered one of the most promising candidates for future energy sources.[1−4] Among the numerous hydrogen production technologies, electrocatalytic water splitting has garnered widespread attention due to its environmental friendliness and its capability for the scalable production of high-purity hydrogen.[5−8] This process primarily consists of two half-reactions: the oxygen evolution reaction (OER) and the hydrogen evolution reaction (HER). However, the OER involves a complex four-electron transfer process, which results in sluggish kinetics and requires a high overpotential, thereby severely limiting the overall efficiency of water splitting.[9−12] Currently, precious metal-based catalysts, such as IrO_2, RuO_2, and Pt/C, exhibit excellent performance in OER and HER. Nevertheless, their high cost, scarcity, and insufficient stability hinder their large-scale industrial application.[13−16] To address these issues, a variety of effective and low-cost electrocatalysts have been successfully developed, including transition metal oxides, nitrides, sulfides, phosphides, selenides, and (oxy)hydroxides.[17−21] In recent years, among transition metal-based materials, Layered Double Hydroxides (LDHs) in particular have become a research hotspot for nonprecious metal catalysts, widely applied in the oxygen evolution reaction (OER) due to their abundant raw material sources, low cost, tunable electronic structures, and good electrocatalytic activity.[22−24] Among them, NiFe-LDHs, owing to their unique layered structure and adjustable metal ratios, exhibit excellent catalytic performance and stability, and are considered one of the most promising OER catalysts with potential for industrialization.[25,26] However, LDH materials still face numerous challenges. For

Received: July 8, 2025
Revised: September 13, 2025
Accepted: September 15, 2025

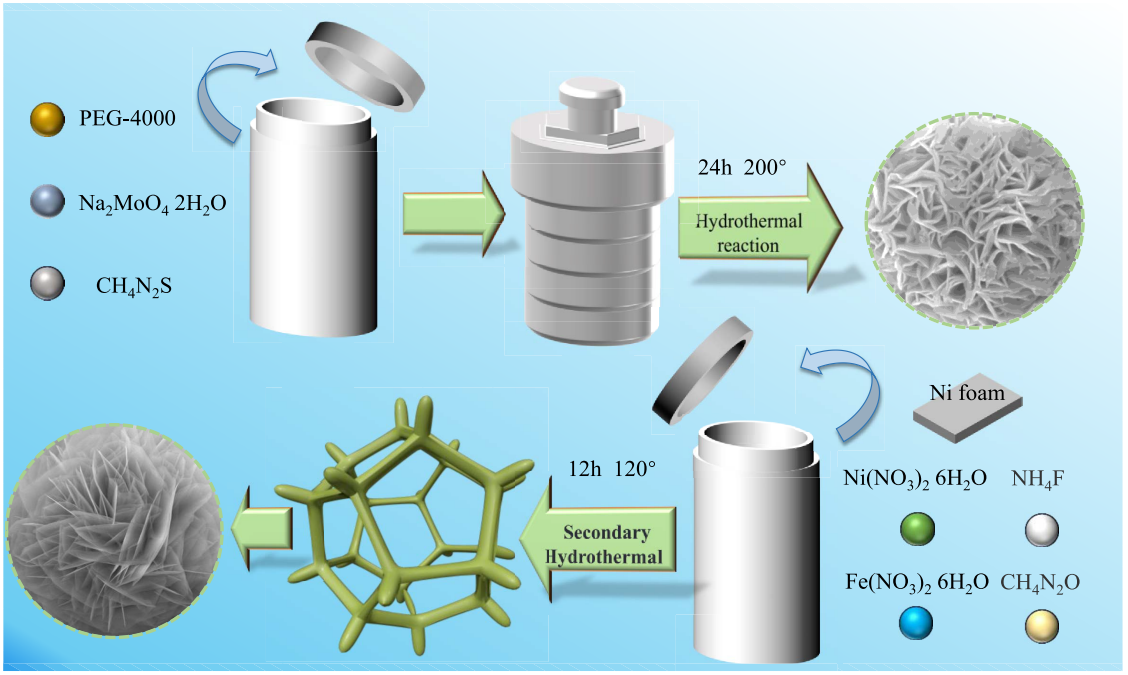

Figure 1. Process of NiFe-LDH/MoS_2/NF preparation.

instance, their lamellar structures are prone to restacking, which leads to a reduced specific surface area and insufficient exposure of active sites, thereby limiting effective contact with the electrolyte. Concurrently, their poor electrical conductivity affects electron transport efficiency, hindering further improvements in catalytic performance.[27,28] Furthermore, their inferior HER performance is also a major drawback for overall water splitting. To address these challenges, researchers have implemented several effective modifications. For example, Lu's team successfully tuned the electronic structure of the material by introducing an appropriate amount of tetravalent manganese (Mn^{4+}) into the LDH layers, significantly enhancing the catalytic activity and stability of the ternary NiFeMn-LDH in the OER.[29] Feng et al. proposed a bifunctional electrocatalyst with markedly improved performance, constructed based on a typical three-dimensional hierarchical NiFe LDH heterostructure.[30] Meanwhile, MoS_2 is an effective HER catalyst and has shown broad application prospects in the field of catalysis due to its large specific surface area, abundant catalytically active sites, excellent chemical stability, and tunable surface properties.[31,32] However, its nonideal adsorption energy for hydroxyl (OH) groups can lead to a decrease in overall water splitting efficiency. Current research indicates that constructing heterostructure interfaces can effectively modulate the energy barriers at the edge sites of MoS_2, thereby enhancing its water splitting performance.[33,34] For instance, Yang et al. successfully prepared MoS_2−Ni_3S_2 heterostructured composite nanorods on nickel foam (NF) via a hydrothermal method. This material exhibited significantly superior OER catalytic performance compared to single-component MoS_2 and Ni_3S_2.[35] Therefore, to overcome the inherent drawbacks of single-component materials, such as the poor electrical conductivity of NiFe-LDH and the suboptimal oxygen evolution reaction (OER) performance of MoS_2, this study proposes a strategy to construct a NiFe-LDH/MoS_2 heterostructure.

Currently, many studies fabricate MoS_2/NiFe-LDH heterostructures by electrochemically depositing MoS_2 nanoparticles onto exfoliated NiFe-LDH nanosheets or by constructing hierarchical architectures on carbon fiber paper (CFP) to enhance catalytic performance. Additionally, some efforts have focused on growing NiFe-LDH/MoS_2 composites on nickel foam via multistep hydrothermal processes. Although this enables direct growth on conductive substrates, it suffers from long reaction durations and limited morphological control. Moreover, most of these studies evaluate performance at low current densities (e.g., 10−100 mA cm^{-2}), which poorly reflect the catalyst's behavior under practical operating conditions.[36−38] In contrast, this work reports the first in situ construction of a rose-like NiFe-LDH/MoS_2 heterostructure on nickel foam via a simple two-step hydrothermal approach. The unique three-dimensional hierarchical morphology significantly enhances active site exposure and facilitates electrolyte diffusion and gas evolution, contributing to improved catalytic efficiency. Furthermore, the as-prepared catalyst exhibits outstanding bifunctional electrocatalytic activity, with exceptional OER performance-requiring only a 376 mV overpotential to achieve a current density of 1000 mA cm^{-2} in 1.0 M KOH, a benchmark for industrial-scale water splitting. In overall water splitting applications, the voltage required to drive 10 mA cm^{-2} is as low as 1.49 V in alkaline freshwater and only 1.53 V in alkaline seawater. This work will systematically evaluate the performance of this catalyst and, by combining experimental XPS characterization with theoretical DFT calculations, deeply investigate the synergistic mechanism behind its excellent performance.

2. EXPERIMENTAL SECTION

2.1. Synthesis of MoS_2 Catalysts. The MoS_2 powder was prepared through a facile hydrothermal route. For the synthesis, 1.8 g of sodium molybdate dihydrate ($Na_2MoO_4{\cdot}2H_2O$), 2.6 g of thiourea (CH_4N_2S), and 0.17 g of polyethylene glycol-4000 (PEG-4000) were used as starting materials. These precursors were added to 50 mL of deionized water (DW) and stirred for 40 min to ensure thorough mixing. Subsequently, the mixture was sealed in a Teflon-lined stainless steel autoclave and heated at 200 °C for 24 h. After cooling to room

https://doi.org/10.1021/acs.cgd.5c01006
Cryst. Growth Des. XXXX, XXX, XXX−XXX

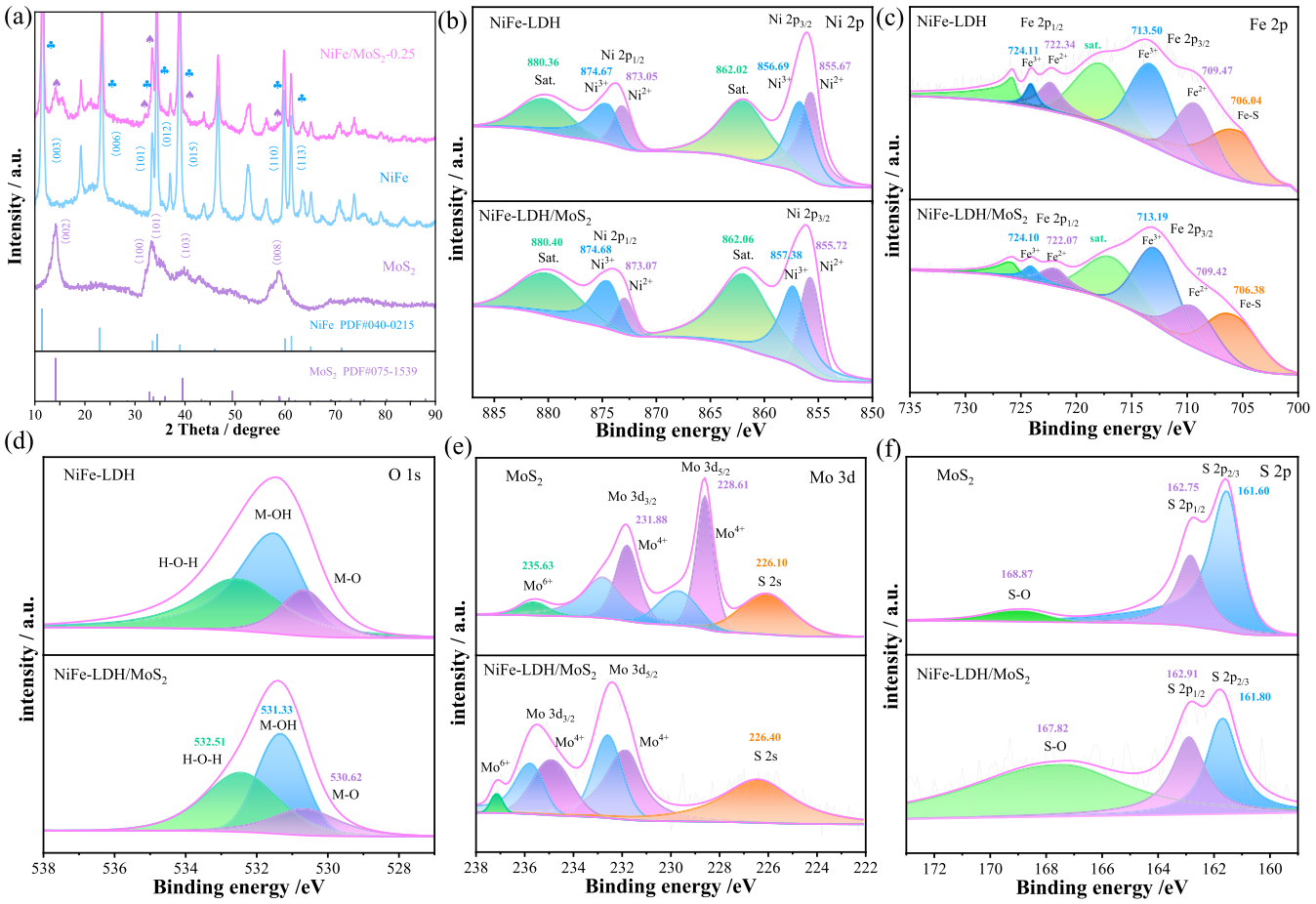

Figure 2. Structure Characterization of As-Fabricated Samples (a) XRD Patterns (b) XPS of Ni 2p (c) Fe 2p (d) O 1s (e) Mo 3d (f) S 2p.

temperature, washing with deionized water and ethanol several times. The final MoS_2 product was obtained after drying at 60 °C.

2.2. Synthesis of NiFe-LDH/MoS_2/NF. First, the nickel foam (NF, 5 × 5 cm^2) substrate was pretreated by sequential sonication in 3.0 M HCl, absolute ethanol, and deionized water to eliminate the surface oxide layer. For the synthesis of the NiFe-LDH/MoS_2 heterostructures, the pretreated NF was used as a substrate for in situ growth. The reaction precursors, including 2.4 mmol of $Ni(NO_3)_2{\cdot}6H_2O$, 0.8 mmol of $Fe(NO_3)_3{\cdot}9H_2O$, 12 mmol of urea, 9 mmol of NH_4F, and a specific mass (x) of presynthesized MoS_2 powder (where x = 0.2, 0.25, and 0.3), were dissolved in 60 mL deionized water. The pretreated NF was then fully immersed in the above solution, which was subsequently transferred to a stainless steel autoclave and heated at 120 °C for 12 h. The product-loaded NF was rinsed with absolute ethanol and deionized water more than three times and then dried. The final samples were named NiFe-LDH, NiFe-LDH/MoS_2-0.2, NiFe-LDH/MoS_2-0.25, and NiFe-LDH/MoS_2-0.3, corresponding to the amount of MoS_2 added (x = 0, 0.2, 0.25, and 0.3 g), respectively.

2.3. Physical Characterization. The phase composition and crystal structure of the as-prepared samples were investigated by X-ray diffraction (XRD) using a Shimadzu-7000 diffractometer with Cu Kα radiation (λ = 0.1541 nm, 40 kV). X-ray photoelectron spectroscopy (XPS) measurements were performed on an ESCALAB 250 instrument with an Al Kα X-ray source to analyze the elemental composition and surface chemical valence states of the materials. The surface morphology and microstructure of the samples were systematically characterized using a scanning electron microscope (SEM, Gemini 300-71-31).

2.4. Electrochemical Testing. All electrochemical measurements were conducted on a CHI760E electrochemical workstation. Electrochemical measurements were carried out in a standard three-electrode configuration using either 1 M KOH (pH = 13.7) or 1 M KOH prepared from natural seawater (pH = 13.51) as the electrolyte. In this setup, the as-prepared sample served as the working electrode, an Hg/HgO electrode was used as the reference electrode, while a platinum (Pt) foil and a carbon rod were used as the counter electrodes for the oxygen evolution reaction (OER) and hydrogen evolution reaction (HER), respectively. The electrochemical performance was evaluated through cyclic voltammetry (CV), linear sweep voltammetry (LSV), electrochemical impedance spectroscopy (EIS), and chronoamperometric (i–t) stability tests. All LSV curves were corrected with 90% iR compensation. The LSV scans were performed at a rate of 2 mV s^{-1} for OER and 5 mV s^{-1} for HER. The electrochemically active surface area (ECSA) was determined from the double-layer capacitance (C_{dl}), which was derived from CV measurements conducted at various scan rates (10–50 mV s^{-1}). All potentials were converted to the reversible hydrogen electrode (RHE) scale using the following equation: $E_{(vs\ RHE)} = E_{(vs\ Hg/HgO)} + 0.059 \times pH + 0.098$ V. Furthermore, the overall water splitting performance was evaluated in a two-electrode system with a corresponding scan rate of 5 mV s^{-1}.

3. RESULTS AND DISCUSSION

Figure 1 presents a schematic diagram of the synthesis process of NiFe-LDH/MoS_2/NF, following the experimental steps described above. The crystal structure and phase composition of the materials were characterized by X-ray diffraction (XRD). To eliminate the influence of the substrate, all samples were collected as powders from the nickel foam substrate via sonication prior to the XRD measurements. Figure 2a displays the XRD patterns of the as-synthesized MoS_2, NiFe-LDH, and the NiFe-LDH/MoS_2-0.25 composite, which are compared with their corresponding standard JCPDS cards. The excellent match

https://doi.org/10.1021/acs.cgd.5c01006
Cryst. Growth Des. XXXX, XXX, XXX−XXX

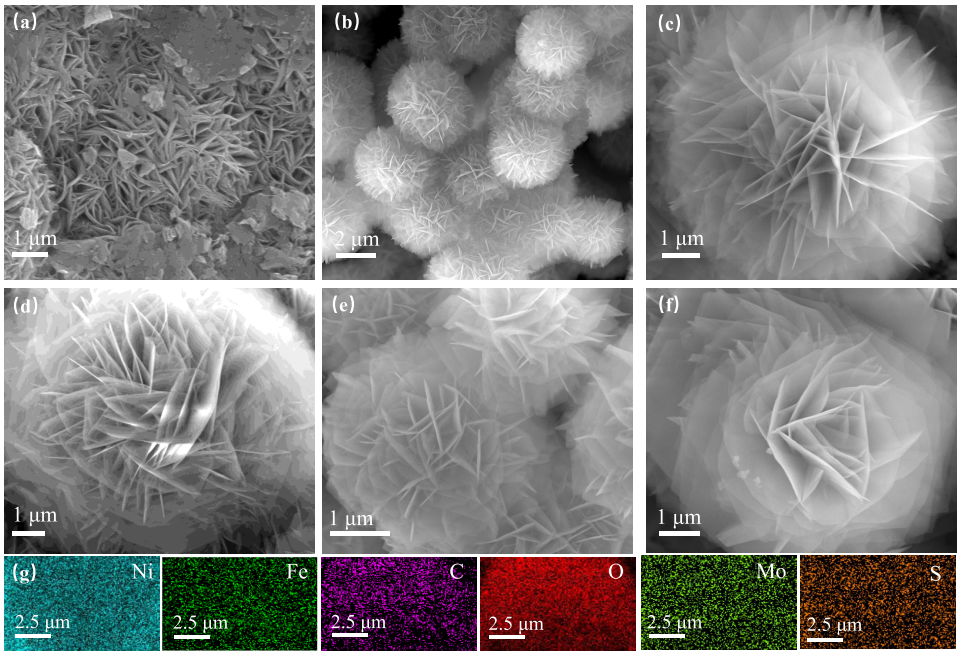

Figure 3. Morphology and structural characteristics of the prepared sample (a) SEM images of MoS_2 samples (b) SEM images of NiFe-LDH samples (c) SEM images of NiFe-LDH/MoS_2-0.2 samples (d) SEM images of NiFe-LDH/MoS_2-0.25 samples (e) SEM images of NiFe-LDH/MoS_2-0.3 samples (f) SEM image of the NiFe-LDH/MoS_2-0.25 sample after OER cycling (g) Elemental mapping of NiFe LDH/MoS_2-0.25 samples.

between the patterns of the individual components and their standard cards indicates that the samples possess good crystallinity. In the pattern of the NiFe-LDH/MoS_2-0.25 composite, the characteristic diffraction peaks located at 11.4, 23.0, 33.5, 34.4, 39.0, 59.9, and 61.3° correspond to the (003), (006), (101), (012), (015), (110), and (113) crystal planes of the NiFe-LDH hydrotalcite structure (JCPDS NO. 40-0215), respectively. Furthermore, the remaining characteristic peaks at 14.1, 32.9, 33.7, 39.5, and 58.9° are attributed to the (002), (100), (101), (103), and (008) planes of MoS_2 (JCPDS NO. 75-1539). These XRD results confirm the successful synthesis of the NiFe-LDH/MoS_2-0.25 composite material. Additionally, XRD analysis was conducted on the NiFe-LDH/MoS_2 composites with varying MoS_2 contents, with the results shown in Figure S1a. As can be seen, MoS_2 was successfully incorporated into the composites at all tested ratios. With an increasing amount of added MoS_2, the intensity of its characteristic diffraction peaks becomes progressively stronger and more pronounced, suggesting an enhancement in both the crystalline quality and the relative content of the MoS_2 phase.

X-ray photoelectron spectroscopy (XPS) was employed to characterize the elemental composition and surface electronic structure of the samples, providing an in-depth analysis of the existing forms and chemical valence states of each element. Prior to data analysis, all spectra were calibrated using the C 1s peak at 284.8 eV as a reference. The survey spectra of NiFe-LDH, MoS_2, and NiFe-LDH/MoS_2 are presented in Figure S1b, revealing the presence of Ni, Fe, Mo, S, and O elements. As depicted in the high-resolution Ni 2p spectrum in Figure 2b, the peaks located at 857.38 and 855.72 eV are assigned to the Ni $2p_{3/2}$ spin−orbit peaks of Ni^{3+} and Ni^{2+} in the NiFe-LDH/MoS_2-0.25 composite, respectively. Meanwhile, the characteristic peaks at 874.68 and 873.06 eV correspond to the Ni $2p_{1/2}$ spin−orbit peaks of Ni^{3+} and Ni^{2+}, respectively. The two peaks at 862.06 and 880.40 eV are satellite peaks (labeled "sat."). These results indicate the coexistence of both Ni^{3+} and Ni^{2+} ions in the NiFe-LDH. Notably, compared to pristine NiFe-LDH, the Ni 2p spectrum of the NiFe-LDH/MoS_2-0.25 composite exhibits a positive shift in its binding energy peaks. This phenomenon suggests a strong electronic interaction between MoS_2 and NiFe-LDH, which likely originates from the coupling effect between them, further confirming the successful construction of the composite structure.[39] As shown in Figure 2c, the high-resolution Fe 2p spectrum of NiFe-LDH/MoS_2-0.25 can be deconvoluted into several peaks. The characteristic peaks at 713.19 and 724.10 eV correspond to the Fe $2p_{3/2}$ and Fe $2p_{1/2}$ orbitals of Fe^{3+}, respectively. Concurrently, a satellite peak attributed to Fe^{3+} is observed at 717.22 eV. Furthermore, the peaks at 709.42 and 722.07 eV can be assigned to the Fe $2p_{3/2}$ and Fe $2p_{1/2}$ orbitals of Fe^{2+}, respectively.[40] The characteristic peak located at 706.04 eV is associated with the Fe−S bond.[41] As shown in Figure 2d, the O 1s spectrum exhibits three characteristic peaks at 530.62, 531.33, and 532.51 eV, which are assigned to metal−oxygen (M−O) bonds, metal−hydroxyl (M−OH) groups in the layered double hydroxide, and H−O−H structures in surface-adsorbed water molecules, respectively.[42,43] The prominent M−OH peak indicates a hydroxyl-rich surface, a key feature contributing to the high OER activity of LDH-based materials. These M−OH groups are widely regarded as the initial active sites for OER, facilitating OH^- adsorption from the electrolyte and promoting the first proton-coupled electron transfer (PCET) step (M−OH + $OH^- \rightarrow$ M-O + H_2O + e^-), thereby lowering the reaction kinetic barrier. Moreover, the M−OH species participate in the formation of critical oxygen-containing intermediates (e.g., *O and *OOH), while their interconnected hydrogen-bonding network enables rapid proton transport (proton hopping), which accelerates the overall reaction kinetics. As illustrated in Figure 2e, the Mo 3d spectrum of pristine MoS_2 exhibits three characteristic peaks at 235.63, 231.88, and 228.61 eV. These peaks correspond to the Mo $3d_{3/2}$ and Mo $3d_{5/2}$ orbitals of Mo^{4+} and the presence of Mo^{6+}, respectively. The emergence of Mo^{6+} is attributed to the formation of Mo−O bonds from the

https://doi.org/10.1021/acs.cgd.5c01006
Cryst. Growth Des. XXXX, XXX, XXX−XXX

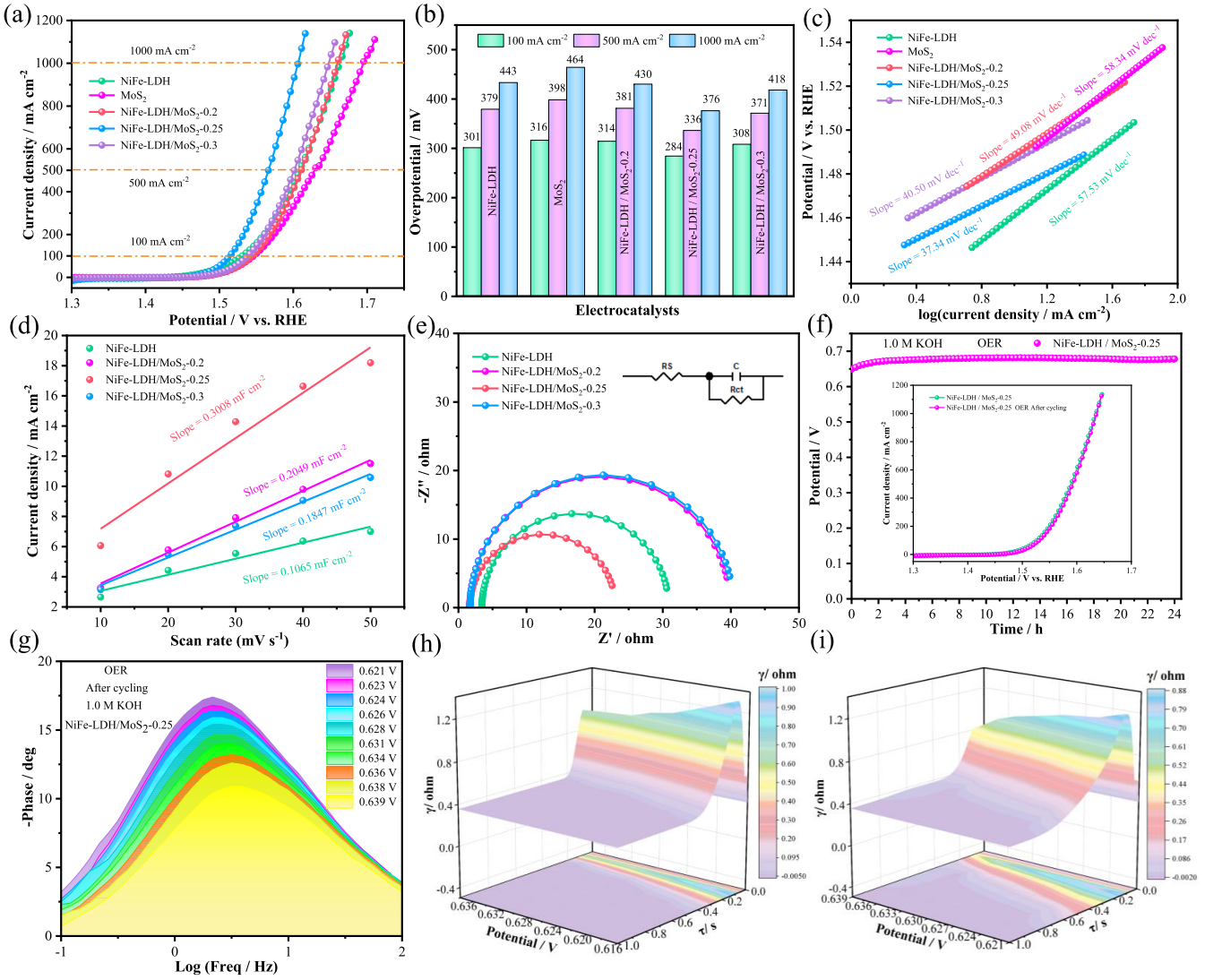

Figure 4. OER performance in 1.0 M KOH (a) LSV curves at scan rate of 2 mV s^{-1} (b) overpotential of the catalyst (c) Tafel plots (d) double-layer capacitance (C_{dl}) CV curves at different scan rates (e) Nyquist plots (f) Chronopotentiometric stability curve (g) Bode plot of NiFe-LDH/MoS_2-0.25 sample after cycling at multiple voltages (h) DRT plot of NiFe-LDH/MoS_2-0.25 before OER cycling (i) DRT plot of NiFe-LDH/MoS_2-0.25 after OER cycling.

unavoidable surface oxidation of the material in air.[44] Additionally, the peak at 226.10 eV is assigned to the Mo−S bond signal near the S 2s orbital. For the NiFe-LDH/MoS_2-0.25 composite, the binding energies of the Mo $3d_{3/2}$ and Mo $3d_{5/2}$ peaks show a positive shift to higher binding energies. This indicates an electron transfer from MoS_2 to NiFe-LDH at the heterointerface, further confirming the strong electronic interaction between the two components. Figure 2f displays the S 2p spectrum of NiFe-LDH/MoS_2-0.25. The spin−orbit peak at 162.91 eV (S $2p_{1/2}$) is attributed to metal−sulfur bonds such as Fe−S and Ni−S. Meanwhile, the peak at 161.80 eV (S $2p_{3/2}$) indicates the presence of low-coordination sulfur ions, suggesting the existence of active sulfur sites within the material.[45] Furthermore, the peak at 167.82 eV corresponds to surface-oxidized sulfur species, which further reveals the strong electronic effect within the catalyst.[46]

Subsequently, the surface morphologies of the catalysts were further characterized using scanning electron microscopy (SEM). Figure 3a reveals the morphology of MoS_2, indicating that its structure is composed of both nanosheets and nanoblocks. In the loose regions, the nanosheets are interlaced with each other, fully exposing their highly active edges. In contrast, the dense regions are formed by the fusion of highly stacked nanosheets, creating thick, block-like structures. Figure 3b displays the morphology of NiFe-LDH. On the whole, the material is composed of multiple, regularly arranged nanospheres. These nanospheres are not solid but are formed by a large number of interconnected nanosheets. This unique structure not only facilitates the exposure of more active sites but also promotes the diffusion of electrolyte and charge transfer, thereby effectively enhancing the catalytic performance of the material. Figure 3c−e present the SEM images of the NiFe-LDH/MoS_2 heterostructures formed with different MoS_2 loading contents. It can be observed that they all form rose-like heterostructures composed of numerous nanosheets. Each "petal" appears to be made of thin, flake-like nanomaterials that radiate outward from a central point, creating a flower-like morphology. This structure not only increases the material's specific surface area but may also provide more active sites, facilitating catalytic reactions. In the NiFe-LDH/MoS_2-0.25

https://doi.org/10.1021/acs.cgd.5c01006
Cryst. Growth Des. XXXX, XXX, XXX−XXX

heterostructure, a greater number and denser distribution of nanosheets are observed. This implies that at this specific loading concentration, the resulting nanosheets are not only more abundant in quantity but are also more compactly arranged, forming a higher-density structure. Figure 3f shows the SEM image of the NiFe-LDH/MoS_2-0.25 sample after OER cycling in 1.0 M KOH. As can be seen, the structural features of the sample remain largely unchanged, still preserving the rose-like heterostructure composed of numerous nanosheets. This indicates that the NiFe-LDH/MoS_2-0.25 catalyst possesses excellent structural stability. Figure 3g presents the elemental mapping analysis results of the NiFe-LDH/MoS_2-0.25 sample, showing that the six elements—Ni, Fe, C, O, Mo, and S—are uniformly distributed throughout the material. This further confirms the successful synthesis and preparation of the NiFe-LDH/MoS_2-0.25 sample. Research has shown that nanomaterials with micro/nanoscale asymmetric heterojunctions can exhibit many unique properties that are not present in homogeneous materials or symmetric nanostructures.[47] The nitrogen adsorption−desorption isotherms of the samples are shown in Figure S2a. All three samples exhibit typical type IV isotherms with H3-type hysteresis loops, indicating the presence of mesoporous structures formed by the stacking of nanosheets. The BET specific surface area analysis reveals that the specific surface areas of NiFe-LDH/MoS_2-0.25, NiFe-LDH, and MoS_2 are 7.97, 3.87, and 1.84 $m^2 g^{-1}$, respectively. The corresponding pore size distribution curves (Figure S2b) indicate that both the average pore volume (0.0005 $cm^3 g^{-1}$) and average pore size (24.38 nm) of NiFe-LDH/MoS_2-0.25 are larger than those of NiFe-LDH (0.00048 $cm^3 g^{-1}$, 17.62 nm) and MoS_2 (0.0002 $cm^3 g^{-1}$, 13.28 nm). These BET results are consistent with the SEM analysis, confirming that the rose-like heterostructure composed of numerous nanosheets possesses a rich porous architecture. This structure not only increases the material's specific surface area but also likely provides a greater number of active sites, thereby enhancing the material's electrocatalytic performance.

To evaluate the electrocatalytic activity of the materials, their Oxygen Evolution Reaction (OER) performance was first investigated in an alkaline electrolyte (1.0 M KOH). As shown in Figure 4a, the NiFe-LDH/MoS_2-0.25 catalyst exhibits lower overpotentials at current densities of 100, 500, and 1000 mA cm^{-2} compared to the other catalysts, demonstrating superior OER performance. Specifically, as detailed in Figure 4b, the NiFe-LDH/MoS_2-0.25 catalyst requires an overpotential of only 284 mV to reach 100 mA cm^{-2}. Even at industrial-grade current densities of 500 and 1000 mA cm^{-2}, it only requires OER overpotentials of 336 mV and 376 mV, respectively. These values are significantly lower than those for the NiFe-LDH (301, 379, and 443 mV @ 100, 500, and 1000 mA cm^{-2}), MoS_2 (316, 398, and 464 mV @ 100, 500, and 1000 mA cm^{-2}), NiFe-LDH/MoS_2-0.2 (314, 381, and 430 mV @ 100, 500, and 1000 mA cm^{-2}), and NiFe-LDH/MoS_2-0.3 (308, 371, and 418 mV @ 100, 500, and 1000 mA cm^{-2}) catalysts. Evidently, compared to the base catalysts and the heterostructures with different MoS_2 loadings, the NiFe-LDH/MoS_2-0.25 heterostructure not only shows potential for industrial application but also displays enhanced catalytic performance. This significantly enhanced activity of NiFe-LDH/MoS_2-0.25 highlights the crucial role played by the formation of the heterostructure and the synergistic effect between NiFe-LDH and MoS_2. Figure 4c further analyzes the Tafel slope, an indicator of reaction kinetics, which was derived from the LSV curves. The NiFe-LDH/MoS_2-0.25 catalyst exhibits the smallest Tafel slope (37.34 mV dec^{-1}), a value lower than that of NiFe-LDH (57.53 mV dec^{-1}), MoS_2 (58.34 mV dec^{-1}), NiFe-LDH/MoS_2-0.2 (49.08 mV dec^{-1}), and NiFe-LDH/MoS_2-0.3 (40.05 mV dec^{-1}). This result suggests a possible synergistic effect between NiFe-LDH and MoS_2, which endows the catalyst with rapid charge transport capabilities and an efficient electron transfer process, significantly boosting the OER catalytic performance. Furthermore, to additionally evaluate the electrocatalytic activity, the electrochemically active surface area (ECSA) can be used as a standard metric. Although direct comparison is limited by factors such as different ECSA collection intervals and nonlinear current distortions, the ECSA can be estimated from the double-layer capacitance (C_{dl}) values obtained from CV curves to assess the intrinsic activity of the material. The double-layer capacitance (C_{dl}) is directly proportional to the ECSA (ECSA = C_{dl}/C_s), where a higher C_{dl} value implies a larger ECSA and more exposed active sites, thereby enhancing catalytic performance.[48] Accordingly, the C_{dl} values in Figure 4d were obtained from the CV plots in Figure S3a−d. As seen in Figure 4d, the C_{dl} value of NiFe-LDH/MoS_2-0.25 (0.301 mF cm^{-2}) is higher than that of NiFe-LDH (0.107 mF cm^{-2}), NiFe-LDH/MoS_2-0.2 (0.205 mF cm^{-2}), and NiFe-LDH/MoS_2-0.3 (0.185 mF cm^{-2}). This further demonstrates the performance enhancement endowed by the incorporation of MoS_2. Electrochemical impedance spectroscopy (EIS) was utilized to investigate the kinetic behavior of the catalysts during the oxygen evolution reaction (OER). By fitting the Nyquist plots with an equivalent circuit, the charge transfer resistance (R_{ct}) and solution resistance (R_s) can be obtained. The R_{ct}, determined by the diameter of the semicircle in the low-frequency region, reflects the charge transfer efficiency between the catalyst and the electrolyte. A smaller semicircle radius corresponds to a lower R_{ct}, indicating faster charge transfer, more favorable reaction kinetics, and higher catalytic activity. As shown in Figure 4e and Table S1, NiFe-LDH/MoS_2-0.25 exhibits the smallest R_{ct} value (21.39 Ω) and R_s value (1.682 Ω), which suggests that this catalyst possesses excellent electrical conductivity. It is noteworthy that the NiFe-LDH/MoS_2-0.25 catalyst displays both a low R_{ct} value and a small Tafel slope, indicating that its OER kinetics are faster than those of the single-component NiFe-LDH catalyst and revealing a pronounced synergistic effect. This signifies an enhanced charge transfer rate between the electrode and the electrolyte, reflecting the beneficial impact of MoS_2 incorporation on both the conductivity and the overall electrochemical performance. This synergistic effect is further supported by the positive shift observed in the Ni 2p XPS spectrum of the NiFe-LDH/MoS_2-0.25 catalyst. After modification with MoS_2, the enrichment of empty d-orbitals on the Ni sites facilitates a stronger binding with OH* intermediates, thereby boosting the OER activity.[49] The loading of MoS_2 is a critical parameter that governs the catalytic performance of the NiFe-LDH. This study investigated the effect of different MoS_2 loadings on the material's properties, revealing that NiFe-LDH/MoS_2-0.25 exhibits the best OER activity. As the MoS_2 amount was increased from 0.2 to 0.25 g, the catalytic activity was significantly enhanced. This improvement is attributed to the formation of a denser and more uniform rose-like structure with an increased specific surface area, evidenced by its double-layer capacitance reaching a maximum value (0.301 mF cm^{-2}) while the charge transfer resistance decreased to 21.39 Ω. These results indicate a greater number of active sites and more efficient electron transport. Upon further increasing the loading to 0.3 g, a decline in catalytic performance was observed, with

https://doi.org/10.1021/acs.cgd.5c01006
Cryst. Growth Des. XXXX, XXX, XXX−XXX

the overpotential at a current density of 1000 mA cm^{-2} increasing from 376 to 418 mV. This performance degradation correlates with the sharp decrease in the C_{dl} value (to 0.185 mF cm^{-2}) and a rise in R_{ct}, suggesting that an excess of MoS_2 may lead to local agglomeration, which partially covers the active sites on the NiFe-LDH surface and hinders both electrolyte diffusion and charge transfer. Therefore, 0.25 g is the optimal loading for MoS_2. At this ratio, the material achieves a synergistic optimization of its morphology, active site exposure, and charge transfer efficiency, thereby constructing a highly efficient and stable catalytic interface for the OER. In addition to excellent catalytic activity, the cycling stability is another crucial criterion for evaluating the performance of a catalyst. Figure 4f displays the results of the chronopotentiometry test for the NiFe-LDH/MoS_2-0.25 catalyst. Following 24 h of prolonged electrolysis, the potential remains nearly constant. Furthermore, the inset in the figure shows the LSV curves before and after the OER cycling test, which remain nearly identical. These results confirm that the as-prepared electrocatalyst exhibits remarkable structural stability and sustained catalytic activity under long-term operating conditions, indicating its excellent cycling stability. Figure S1c presents the Bode plots for NiFe-LDH/MoS_2-0.25 at various potentials, where the change in phase angle with frequency reflects the dynamic response behavior of the catalyst sample.[50] The plots show that as the applied potential increases, the phase angle in the low-frequency region exhibits a systematic decrease. This trend indicates a continuous reduction in the charge transfer resistance (R_{ct}), further illustrating a progressive acceleration of the charge transfer rate. A Bode plot analysis was also performed on the NiFe-LDH/MoS_2-0.25 sample after the cycling stability test (see Figure 4g). The phase angles in this plot still maintain their well-ordered sequence, which further demonstrates that the material possesses excellent and stable charge transport capabilities. The Distribution of Relaxation Times (DRT) is an analytical method used to deconvolute complex impedance signals into multiple individual electrochemical processes. By resolving impedance spectroscopy data, it identifies peaks corresponding to different relaxation times, which respectively reflect kinetic processes with varying rates, such as interfacial charge transfer, ion migration, and double-layer charging.[51−53] Figure 4h visually illustrates the dynamic process of how the material's electrocatalytic activity is activated with increasing applied potential. The main "ridge" peak within the relaxation time (τ) interval of 0.1−1.0 s represents the rate-determining step (RDS) of the OER. This step integrates key kinetic processes including charge transfer (R_{ct}) and the adsorption/conversion of oxygen-containing intermediates. As the potential is increased from 0.616 to 0.632 V, the polarization resistance (γ value) of this RDS sharply decreases, directly demonstrating that the increased overpotential effectively lowers the reaction energy barrier, thereby significantly accelerating the OER rate.[54] Concurrently, the shift of this main peak toward shorter relaxation times and its clear separation from the stable double-layer capacitance process at high frequencies further corroborate this kinetic acceleration.

After the NiFe-LDH/MoS_2-0.25 catalyst underwent a long-term OER stability test, Figure 4i clearly reveals the trend of its performance evolution. Although the polarization resistance (γ value) of the core kinetic process significantly increases, the characteristic relaxation time (τ) shifts to longer durations, and the peak shape becomes broader, the material nevertheless maintains good catalytic activity. In addition, NiFe-LDH/MoS_2-0.25/NF exhibits excellent OER activity at high current densities in 1.0 M KOH, outperforming many recently reported electrocatalysts[55−59] (as shown in Table 1), indicating its broad application prospects in alkaline freshwater electrolysis.

Table 1. OER Performance of the Samples

materials	overpotential (mV)	electrolyte	refs
FeCoNiMnOOH/NF	441/1000 mA cm^{-2}	1.0 M KOH	55
NiFe-LDH/NF	583/1000 mA cm^{-2}	1.0 M KOH	56
CoP@NiFe-LDH/NF	351/400 mA cm^{-2}	1.0 M KOH	57
MoS_2/NF	609/1000 mA cm^{-2}	1.0 M KOH	58
NiCoFe-LDH/NF	499/1000 mA cm^{-2}	1.0 M KOH	59
NiFe-LDH/MoS_2/NF	376/1000 mA cm^{-2}	1.0 M KOH	this study

To evaluate the structural integrity and stability of the material during long-term electrolysis, the NiFe-LDH/MoS_2-0.25 catalyst was characterized by SEM, XRD, and XPS after the chronopotentiometry stability test. As seen in Figure S2c,d, the catalyst retains its rose-like heterostructure composed of numerous nanosheets, indicating that its micromorphology possesses excellent structural stability. In the XRD analysis (Figure S4a), the postreaction sample still clearly displays the characteristic diffraction peaks of both NiFe-LDH and MoS_2, with no significant peak shifts or the formation of new impurity phases, demonstrating that its crystal structure remained stable during the prolonged electrolysis. Figure S4b shows the Ni 2p XPS spectra of the NiFe-LDH/MoS_2-0.25 composite before and after OER cycling. The results reveal that after electrochemical reconstruction, the binding energies of both Ni^{3+} and Ni^{2+} in the Ni 2p spectrum shift to lower energies, a phenomenon closely related to the formation of NiOOH species during the reconstruction process. This change indicates an elevation in the oxidation state of the surface nickel ions and an optimization of the electronic structure, thus heralding an enhancement in the material's oxygen evolution reaction (OER) catalytic activity.[60,61] The Fe 2p spectrum in Figure S4c shows that after reconstruction, both the Fe $2p_{3/2}$ and Fe $2p_{1/2}$ spin−orbit peaks exhibit a slight positive shift. Specifically, the binding energies of Fe^{3+} and Fe^{2+} in the Fe $2p_{3/2}$ orbital shifted to higher energies by 0.06 and 0.50 eV, respectively, while the corresponding Fe^{3+} and Fe^{2+} peak positions in the Fe $2p_{1/2}$ orbital shifted by 0.09 and 0.13 eV, respectively. From the O 1s spectrum (Figure S4d), the decrease in M−O content and the increase in M−OH content after electrochemical reconstruction indicate a dynamic transformation from M−O to M−OH during the OER process. This further confirms the formation of active oxyhydroxide species (NiOOH), which is beneficial for enhancing OER performance. Figure S4e,f show that after electrochemical reconstruction, the characteristic Mo $3d_{3/2}$ and Mo $3d_{5/2}$ peaks attributed to Mo^{4+} are still present, indicating that the basic structure of MoS_2 was retained after the reaction. Additionally, while the signal for Mo^{6+} is still visible, the intensity of the Mo−S bond characteristic peak at 226.12 eV is diminished, and the S−O bond signal at 167.10 eV is enhanced. This suggests that the material's surface underwent unavoidable oxidation during the OER process, leading to the formation of sulfur-oxide species.

The electrocatalytic Hydrogen Evolution Reaction (HER) performance of the catalysts was further investigated in 1.0 M KOH. Figure 5a displays the *iR*-compensated LSV curves of the catalysts for the HER. The NiFe-LDH/MoS_2-0.25 catalyst requires a potential of only 135.7 mV to achieve a current density of −10 mA cm^{-2}, which is lower than that required for NiFe-LDH (161.7 mV @ −10 mA cm^{-2}), NiFe-LDH/MoS_2-0.2

https://doi.org/10.1021/acs.cgd.5c01006
Cryst. Growth Des. XXXX, XXX, XXX−XXX

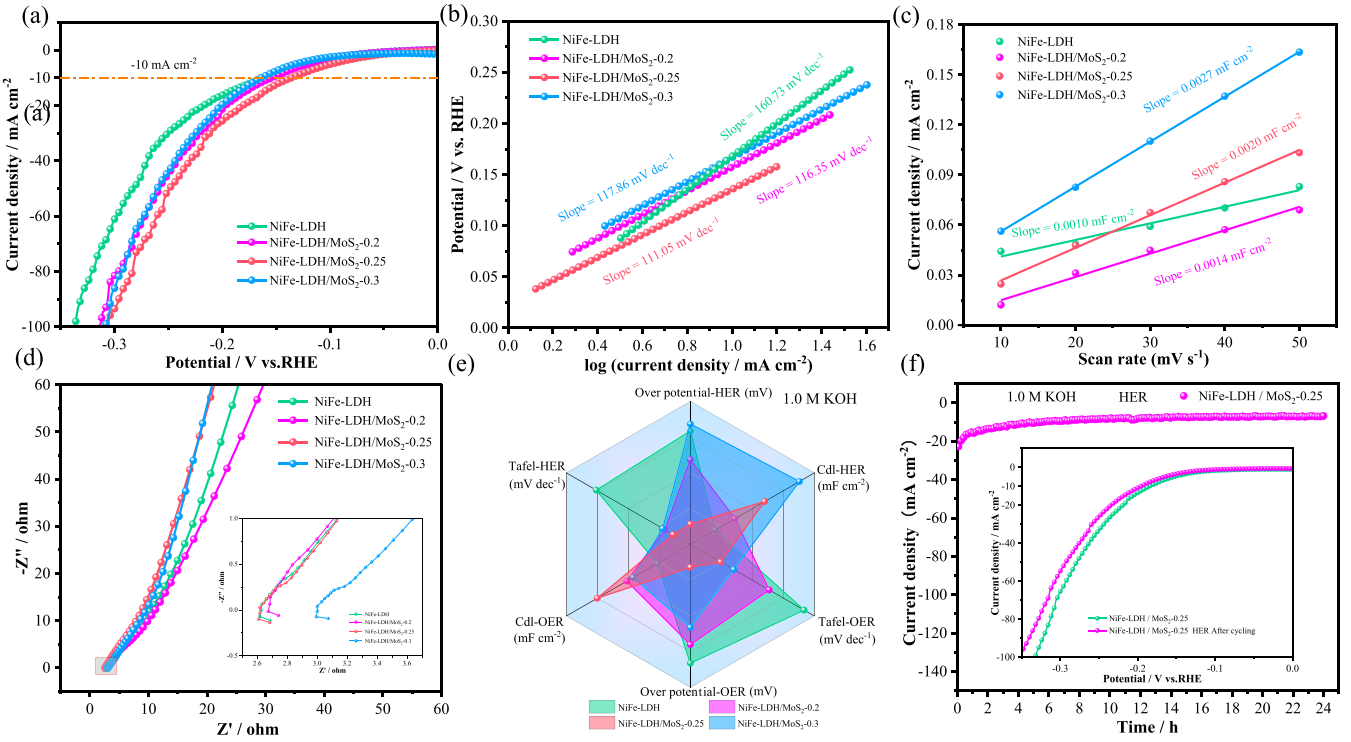

Figure 5. HER performance in 1.0 M KOH (a) LSV curves at scan rate of 5 mV s^{-1} (b) Tafel plots (c) double-layer capacitance (C_{dl}) CV curves at different scan rates (d) Nyquist plots (e) HER and OER radar plot (f) Chronoamperometric stability curves.

(153.7 mV @ −10 mA cm^{-2}), and NiFe-LDH/MoS_2-0.3 (163.7 mV @ −10 mA cm^{-2}). Figure 5b shows the corresponding Tafel plots for the HER. The NiFe-LDH/MoS_2-0.25 catalyst exhibits a Tafel slope of 110.05 mV dec^{-1}, which is smaller than those of the NiFe-LDH (160.73 mV dec^{-1}), NiFe-LDH/MoS_2-0.2 (116.35 mV dec^{-1}), and NiFe-LDH/MoS_2-0.3 (117.86 mV dec^{-1}) catalysts, indicating that NiFe-LDH/MoS_2-0.25 possesses more favorable HER kinetics. In an alkaline electrolyte, the Hydrogen Evolution Reaction (HER) is typically described by the following reaction steps:[62]

$$(\text{Volmer step})H_2O + e^- + M \rightarrow M - H + OH^- \quad (1)$$

$$(\text{Heyrovsky step})M - H + H_2O + e^- \rightarrow H_2 + OH^- + M \quad (2)$$

$$(\text{Tafel step})M - H \rightarrow H_2 + 2M \quad (3)$$

Reported Tafel slopes for the above three steps are 120, 40, and 30 mV dec^{-1}, respectively, indicating that the HER on the NiFe-LDH/MoS_2-0.25 catalyst follows the Volmer−Heyrovsky mechanism ($H_2O + H_{ads} + e^- \rightarrow H_2 + OH^-$). Based on the C_{dl} values derived from Figure 5c, the following trend was observed: NiFe-LDH/MoS_2-0.3 (0.0027 mF cm^{-2}) > NiFe-LDH/MoS_2-0.25 (0.0020 mF cm^{-2}) > NiFe-LDH/MoS_2-0.2 (0.0014 mF cm^{-2}) > NiFe-LDH (0.0010 mF cm^{-2}). These C_{dl} values were obtained from the CV curves shown in Figure S5a−d. The impedance spectroscopy (EIS) test, shown in Figure 5d, further elucidates the electrocatalytic performance of the catalysts. In the low-frequency region, NiFe-LDH/MoS_2-0.25 exhibits the steepest straight-line slope compared to the other catalysts, indicating a lower ion diffusion resistance (Warburg impedance, R_w) which facilitates the rapid diffusion of ions in the electrolyte to the electrode surface. In the high-frequency region, NiFe-LDH/MoS_2-0.25 displays a smaller semicircle diameter, signifying reduced electron and ion transport resistance at the electrode−electrolyte interface and consequently, a lower charge transfer resistance (R_{ct}). Furthermore, the Nyquist plot for this material shows the smallest intercept with the x-axis, further indicating that its hybrid structure possesses the lowest intrinsic resistance (R_s). From the radar plot in Figure 5e, the electrocatalytic performance can be visually assessed using the parameters of overpotential, C_{dl} value, and Tafel slope, based on the enclosed area. It is evident that NiFe-LDH/MoS_2-0.25 demonstrates the optimal catalytic activity for both OER and HER, significantly outperforming the other samples. As shown in Figure 5f, the NiFe-LDH/MoS_2-0.25 material maintained favorable stability throughout a 24-h hydrogen evolution process, indicating its satisfactory structural stability. As shown in Table S2, the HER performance of NiFe-LDH/MoS_2-0.25/NF in 1.0 M KOH is superior to that of various reported electrocatalysts.[63−67]

Currently, most research on hydrogen production via water electrolysis focuses on alkaline freshwater; however, the limited availability of freshwater resources calls for the urgent development of sustainable alternative water sources. Seawater, with its vast reserves, is considered a highly promising solution for direct hydrogen production through electrolysis. Therefore, the OER activity of the synthesized samples was further evaluated in alkaline seawater (1.0 M KOH + seawater, pH = 13.51). As shown in Figure 6a,b, NiFe-LDH/MoS_2-0.25 continues to exhibit excellent OER activity in alkaline seawater. Under these conditions, the catalyst requires overpotentials of only 354 mV, 439 mV, and 493 mV to drive current densities of 100, 500, and 1000 mA cm^{-2}, respectively. Although the overpotential of NiFe-LDH is slightly lower than that of NiFe-LDH/MoS_2-0.25 at current densities of 100 and 500 mA cm^{-2}, NiFe-LDH/MoS_2-0.25 demonstrates superior electrocatalytic performance at the industrially relevant high current density of

https://doi.org/10.1021/acs.cgd.5c01006
Cryst. Growth Des. XXXX, XXX, XXX−XXX

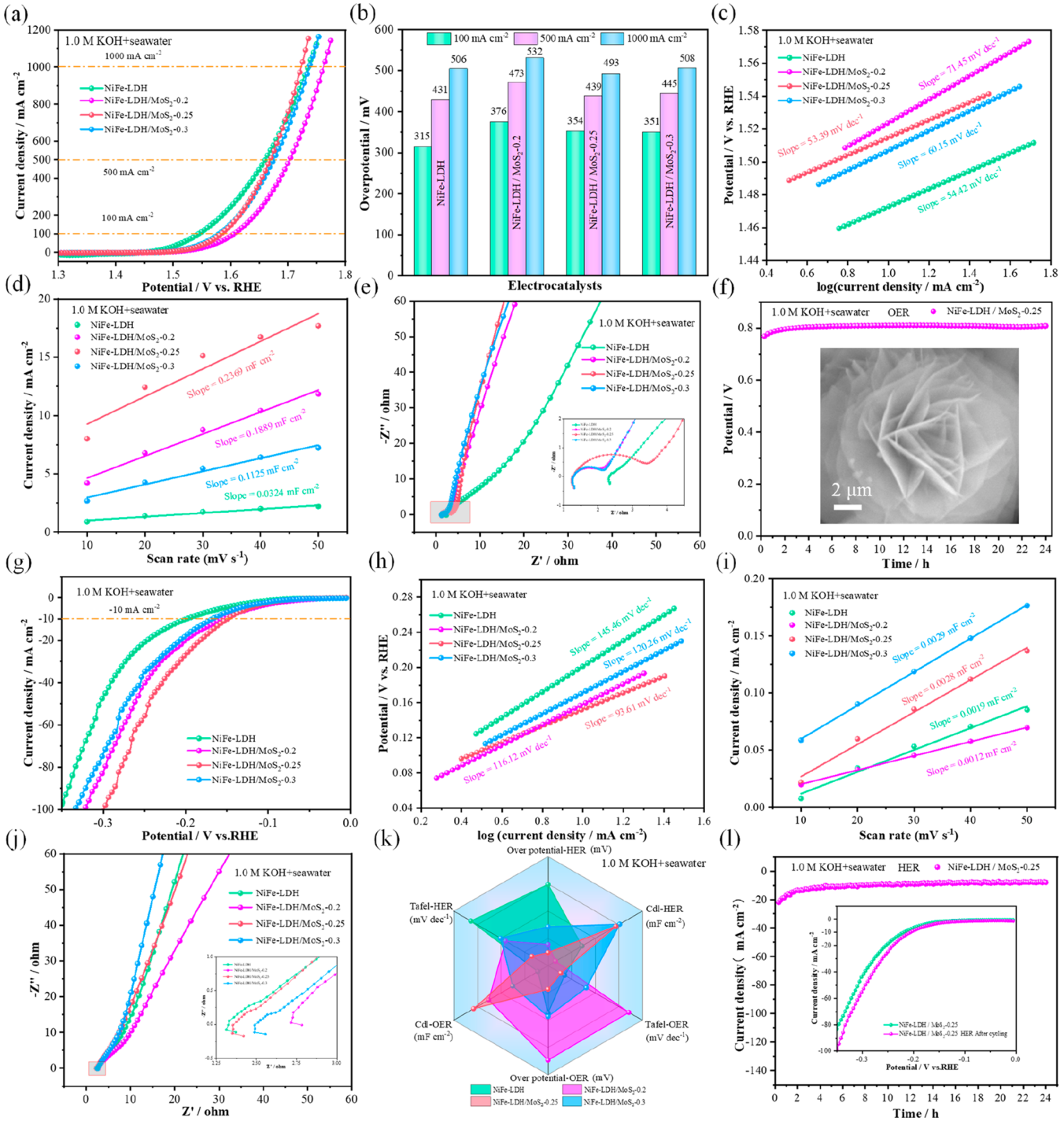

Figure 6. OER and HER performance of the catalyst in 1.0 M KOH with seawater. (a) LSV curves of OER (b) OER overpotential of the catalyst (c) Tafel plots of OER (d) C_{dl} plots of OER (e) Nyquist plots of OER (f) Chronopotentiometric stability curve. (g) LSV curves for HER (h) Tafel plots of HER (i) C_{dl} plots of HER (j) Nyquist plots of HER (k) HER and OER radar plot. (l) Chronoamperometric stability curves.

1000 mA cm^{-2}. Figure 6c indicates that the NiFe-LDH/MoS_2-0.25 catalyst still maintains a low Tafel slope (53.39 mV dec^{-1}) in alkaline seawater, which is lower than that of NiFe-LDH (54.42 mV dec^{-1}), NiFe-LDH/MoS_2-0.2 (71.45 mV dec^{-1}), and NiFe-LDH/MoS_2-0.3 (60.15 mV dec^{-1}). This confirms that NiFe-LDH/MoS_2-0.25 preserves its superior reaction kinetics in alkaline seawater. To further investigate the performance differences among the catalysts, the electrochemically active surface area (ECSA) of each catalyst was calculated based on the cyclic voltammetry (CV) curves at different scan rates (Figure S6a−d), using the double-layer capacitance (C_{dl}) as an evaluation metric. As shown in Figure 6d, NiFe-LDH/MoS_2-0.25 exhibits the highest C_{dl} value (0.2369 mF cm^{-2}), indicating that it possesses a larger electrochemically active surface area, thereby leading to superior catalytic performance. To assess the ion diffusion capability within the materials, electrochemical impedance spectroscopy (EIS) was subsequently performed (Figure 6e). The results show that NiFe-LDH/MoS_2-0.25 has the steepest linear slope in the low-frequency region and the smallest intercept with the real axis in the high-frequency region.

https://doi.org/10.1021/acs.cgd.5c01006
Cryst. Growth Des. XXXX, XXX, XXX−XXX

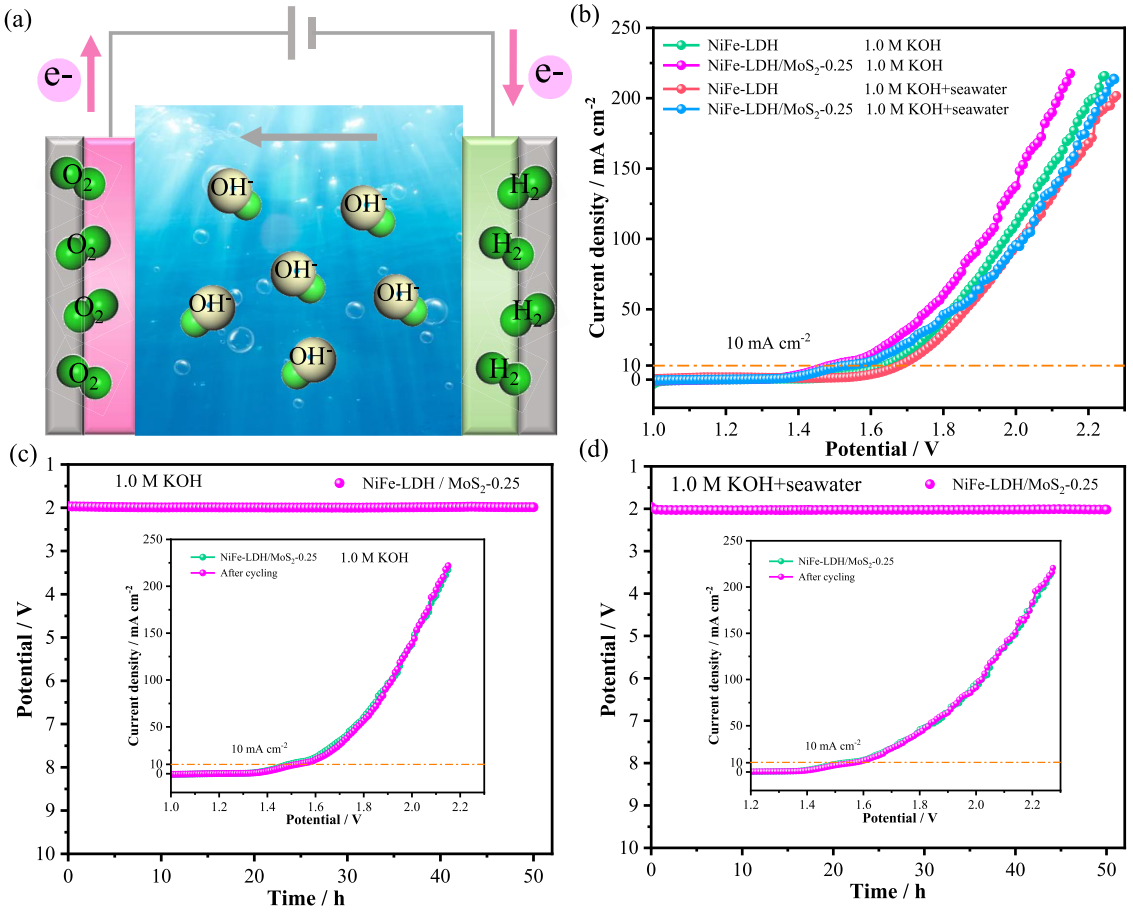

Figure 7. Overall water splitting performance of the electrocatalyst. (a) Schematic diagram of the overall water splitting device. (b) LSV curve. (c) Chronopotentiometric stability curve in 1.0 M KOH (d) Chronopotentiometric stability curve in 1.0 M KOH+ seawater.

This indicates that the sample has a lower ion diffusion resistance and a smaller intrinsic resistance, thus demonstrating superior ion transport properties. Figure 6f showcases the excellent cycling stability of the NiFe-LDH/MoS_2-0.25 catalyst in alkaline seawater. This characteristic signifies that the catalyst can maintain high OER efficiency during long-term operation under alkaline seawater conditions, displaying favorable durability and stability. In summary, although the OER performance of the NiFe-LDH/MoS_2-0.25 catalyst in alkaline seawater is not as high as its performance in alkaline freshwater a decrease in activity primarily attributed to the partial blocking of active sites and surface contamination by ions or particles from the seawater.[68,69] it still demonstrates remarkably excellent catalytic performance and stability. This suggests that the catalyst holds great potential for practical seawater electrolysis applications. Therefore, the development of efficient and stable seawater electrolysis technology is of great significance for alleviating the pressure on freshwater resources and promoting the large-scale production of green hydrogen.

Next, the HER performance of the synthesized catalysts in alkaline seawater was investigated. From the LSV curves in Figure 6g, the overpotentials required to achieve a current density of −10 mA cm^{-2} follow the order: NiFe-LDH/MoS_2-0.25 (149.5 mV) < NiFe-LDH/MoS_2-0.2 (155.5 mV) < NiFe-LDH/MoS_2-0.3 (168.5 mV) < NiFe-LDH (199.5 mV). As seen in Figure 6h, the NiFe-LDH/MoS_2-0.25 catalyst (93.61 mV dec^{-1}) possesses a smaller Tafel slope than the NiFe-LDH sample (145.46 mV dec^{-1}), indicating that the incorporation of MoS_2 can accelerate reaction kinetics and promote high charge transfer efficiency. This result is further corroborated by the ECSA analysis in Figure 6i (calculated from Figure S7a−d). The NiFe-LDH/MoS_2-0.25 catalyst has a higher density of active sites (C_{dl} = 0.0028 mF cm^{-2}), whereas NiFe-LDH has a C_{dl} of 0.0019 mF cm^{-2}. Furthermore, from the electrochemical impedance spectroscopy (EIS) plots in Figure 6j, it is observed that NiFe-LDH/MoS_2-0.3 exhibits a lower ion diffusion resistance, while NiFe-LDH shows a smaller intrinsic resistance. Combining the above analyses with the intuitive representation from the radar plot in Figure 6k, it is clear that the NiFe-LDH/MoS_2-0.25 catalyst is significantly superior to the other comparative samples in terms of overall performance, demonstrating more excellent electrocatalytic activity. This indicates that an appropriate amount of MoS_2 incorporation can significantly enhance its catalytic performance. The results from the chronopotentiometry test (Figure 6l) show that the as-prepared catalyst possesses good stability. The inset displays the LSV curves of the NiFe-LDH/MoS_2-0.25 sample before and after the cycling test. As can be seen, After 24 h of cycling, its overpotential does not show any significant increase, confirming the satisfactory structural stability of the prepared catalyst.

To evaluate the practical application potential of the catalyst in water splitting, its overall water splitting performance was tested in a two-electrode system. As schematically illustrated in Figure 7a, the NiFe-LDH/MoS_2-0.25 on nickel foam samples were used as both the anode and the cathode. The corresponding electrochemical measurements were conducted

https://doi.org/10.1021/acs.cgd.5c01006
Cryst. Growth Des. XXXX, XXX, XXX−XXX

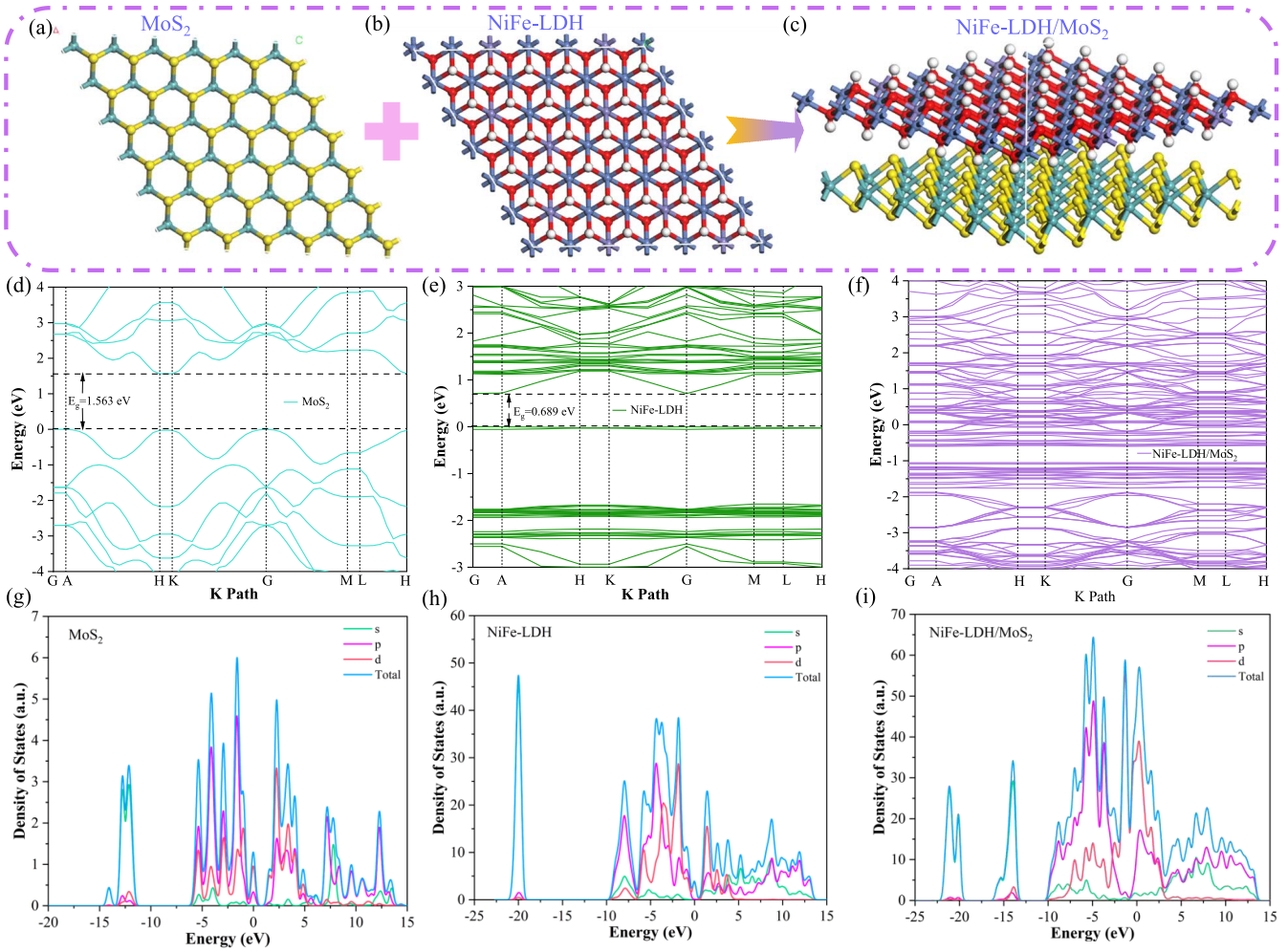

Figure 8. Theoretical simulation and calculation analysis of the catalyst (a) Unit cell models of MoS_2 (b) Unit cell models of NiFe-LDH (c) Unit cell models of NiFe-LDH/MoS_2 (d) Band structure of MoS_2 (e) Band structure of NiFe-LDH (f) Band structure of NiFe-LDH/MoS_2 (g) Density of States (DOS) of MoS_2 (h) Density of States (DOS) of NiFe-LDH (i) Density of States (DOS) of NiFe-LDH/MoS_2.

in 1.0 M KOH and 1.0 M KOH + seawater electrolytes, respectively. In this setup, the oxidation of OH^- to produce O_2 occurs at the anode, while at the cathode, water molecules are reduced to generate H_2. Figure 7b displays the LSV curves of the catalysts recorded at a scan rate of 5 mV s^{-1}. In the 1.0 M KOH electrolyte, the NiFe-LDH/MoS_2-0.25||NiFe-LDH/MoS_2-0.25 electrolyzer requires a cell voltage of only 1.49 V to achieve a current density of 10 mA cm^{-2}, which is significantly lower than the 1.64 V required by the NiFe-LDH||NiFe-LDH couple. In the 1.0 M KOH + seawater electrolyte, the cell voltage for NiFe-LDH/MoS_2-0.25 is 1.53 V at the same current density, which is also superior to the 1.68 V for the NiFe-LDH couple. This demonstrates its excellent overall water splitting performance in different electrolytic environments. As shown in Figure 7c,d, the stability of the NiFe-LDH/MoS_2-0.25 electrolyzer was evaluated in both 1.0 and 1.0 M KOH + seawater electrolytes via chronopotentiometry. After 50 h of cycling, the cell voltage in both cases remained almost constant, demonstrating excellent stability. Furthermore, the insets display the LSV curves measured before and after the durability tests. The results show that the LSV curves are nearly identical, further indicating that the catalyst possesses outstanding structural and performance stability during long-term operation.

To gain in-depth insights into the electronic structure of the electrode materials, Density Functional Theory (DFT) calculations were conducted using the CASTEP module. The Perdew−Burke−Ernzerhof (PBE) exchange-correlation functional, under the Generalized Gradient Approximation (GGA), was employed. The k-point mesh for sampling the Brillouin zone was constructed using the Monkhorst−Pack scheme, and the plane-wave cutoff energy (Ecut) was set to 400 eV. Following geometry optimization for all structures, their band structures and Density of States (DOS) were further calculated. As shown in Figure 8a−c, three models were constructed: MoS_2, NiFe-LDH, and the NiFe-LDH/MoS_2 heterostructure. The energy levels and band gaps of the electrode materials were further investigated via simulations in CASTEP. In Figure 8d−f, the calculated band gap for MoS_2 is 1.563 eV, and for NiFe-LDH, it is 0.689 eV. However, no discernible band gap was observed in the calculated electronic band structure of the NiFe-LDH/MoS_2 heterostructure using the GGA-PBE functional. This is primarily due to the inherent limitations of standard DFT methods for such systems.[70,71] The PBE functional systematically underestimates band gaps due to self-interaction errors and a lack of nonlocal exchange, a deficiency that is particularly pronounced in the strongly correlated d-electron systems of Ni^{2+}/Fe^{3+} in the LDH structure. This intrinsic underestimation of the band gap

https://doi.org/10.1021/acs.cgd.5c01006
Cryst. Growth Des. XXXX, XXX, XXX−XXX

can artificially push the predicted electronic structure toward a metallic or near-zero-gap state. Nevertheless, compared to the individual NiFe-LDH and MoS_2 components, the NiFe-LDH/MoS_2-0.25 composite electrode exhibits a denser distribution of energy bands, suggesting that electrons can migrate more easily between these energy levels, thereby leading to the better catalytic performance of NiFe-LDH/MoS_2-0.25.[72] Simultaneously, the Density of States (DOS) of NiFe-LDH containing MoS_2 was calculated. As seen in Figure 8g, the conduction band (CB) and valence band (VB) of MoS_2 are primarily contributed by the Mo 3d, S 2p, and O 1s orbitals. The presence of lower Mo valence states may be due to the existence of numerous oxygen vacancies on the MoS_2 crystal surface. The valence band of MoS_2 is formed through strong covalent hybridization between the Mo d-orbitals and S p-orbitals, which theoretically explains the nature of the Mo−S chemical bonds observed in the XPS analysis. For NiFe-LDH (Figure 8h), the CB is composed of Fe 2p, Ni 2p, and O 1s states, while the VB is dominated by Fe 2p and Ni 2p states, consistent with the XPS results. As depicted in Figure 8i, the CB of the composite NiFe-LDH/MoS_2 is mainly formed by the hybridization of O 1s, Ni 2p, Fe 2p, and Mo 3d orbitals, while the VB is composed primarily of Ni 2p, Fe 2p, and S 2p orbitals. This indicates a significant reconstruction of the composite's electronic structure, mainly originating from the strong hybridization among the s, p, and d orbitals. This electronic structure modulation, driven by interfacial bonding and charge transfer, fundamentally alters the material's electronic properties, such as its electrical conductivity. The XPS spectra further corroborate the strong interfacial interactions, not only revealing the formation of new chemical bonds like Ni−S and Fe−S but also reflecting the distinct charge redistribution caused by the interfacial coupling. It can also be observed that the DOS value at the Fermi level for the NiFe-LDH/MoS_2 catalyst is significantly higher than that of the NiFe-LDH and MoS_2 electrode materials, suggesting that the NiFe-LDH/MoS_2 catalyst can provide more electrons during the catalytic process. Concurrently, the combination of the two components enhances the density of states near the Fermi level, indicating improved electrical conductivity, which aligns well with the experimental results.

4. CONCLUSIONS

In summary, this study successfully synthesized a rose-like NiFe-LDH/MoS_2 heterostructure catalyst on nickel foam via a simple, one-step hydrothermal method. This unique morphology increases the specific surface area and exposes more active sites, thereby enhancing catalytic performance. In alkaline freshwater, the optimized NiFe-LDH/MoS_2-0.25 catalyst demonstrates excellent bifunctional activity, requiring only 376 mV for the oxygen evolution reaction (OER) at an industrial-grade current density of 1000 mA cm^{-2}, and a low overpotential of just 135.7 mV for the hydrogen evolution reaction (HER) at −10 mA cm^{-2}. This enables overall water splitting at a low cell voltage of 1.49 V (at 10 mA cm^{-2}). Although its activity slightly decreases in alkaline seawater, the catalyst nevertheless maintains remarkable performance, driving an OER current density of 1000 mA cm^{-2} at an overpotential of 493 mV, with a corresponding overall water splitting voltage of 1.53 V. Furthermore, a long-duration continuous electrolysis test of 50 h confirmed the catalyst's excellent operational stability in both electrolytes, highlighting its great potential for practical applications. Both experimental XPS analysis and theoretical DFT calculations collectively reveal that the superior performance of the catalyst originates from the strong electronic interactions and synergistic effects at the NiFe-LDH/MoS_2 heterointerface. The XPS spectra directly confirm the electron transfer and the formation of new chemical bonds across the interface, while DFT calculations indicate that this interaction optimizes the electronic structure by enhancing the Density of States (DOS) near the Fermi level. This synergy ultimately boosts the material's electrical conductivity and electron supply capability, thus fundamentally enhancing its catalytic activity. This work provides a promising strategy for designing efficient and stable catalysts for industrial-scale hydrogen production from both freshwater and seawater.

■ ASSOCIATED CONTENT

Supporting Information

The Supporting Information is available free of charge at https://pubs.acs.org/doi/10.1021/acs.cgd.5c01006.

Figure S1 (XRD patterns, full XPS spectrum, and Bode plot of the samples), Figure S2 (BET isotherms and pore size distribution of the samples, and SEM images after OER cycling), Figure S3 (CV curves of OER in 1.0 M KOH), Figure S4 (XRD patterns and XPS spectra of NiFe-LDH/MoS_2-0.25 before and after OER cycling), Figure S5 (CV curves of HER in 1.0 M KOH), Figure S6 (CV curves of OER in 1.0 M KOH + seawater), Figure S7 (CV curves of HER in 1.0 M KOH + seawater), Table S1 (Electrochemical impedance analysis of the as-obtained samples), and Table S2 (HER performance comparison of the samples) (PDF)

■ AUTHOR INFORMATION

Corresponding Authors

Rong-da Zhao − *School of Chemical & Environmental Engineering, Liaoning University of Technology, Jinzhou, Liaoning 121000, P. R. China;* orcid.org/0000-0002-1637-0909; Email: rongdazhaoln@126.com

Depeng Zhao − *School of New Energy, Shenyang Institute of Engineering, Shenyang, Liaoning 110136, P. R. China;* orcid.org/0000-0001-8054-3926; Email: hellodepeng@163.com

Li-hua Miao − *School of Medical Information Engineering, Shenyang Medical College, Shenyang, Liaoning 110043, P. R. China*; Email: miaolihua@163.com

Authors

Xin Li − *School of Chemical & Environmental Engineering, Liaoning University of Technology, Jinzhou, Liaoning 121000, P. R. China*

Yue Qin − *School of Chemical & Environmental Engineering, Liaoning University of Technology, Jinzhou, Liaoning 121000, P. R. China*

Bo-yang Zhang − *School of Chemical & Environmental Engineering, Liaoning University of Technology, Jinzhou, Liaoning 121000, P. R. China*

Bo-yao Zhang − *School of Chemical & Environmental Engineering, Liaoning University of Technology, Jinzhou, Liaoning 121000, P. R. China*

Jia Li − *School of Chemical & Environmental Engineering, Liaoning University of Technology, Jinzhou, Liaoning 121000, P. R. China*

Complete contact information is available at: https://pubs.acs.org/10.1021/acs.cgd.5c01006

https://doi.org/10.1021/acs.cgd.5c01006
Cryst. Growth Des. XXXX, XXX, XXX−XXX

Author Contributions

[#]X.L. and Y.Q. are co-first authors.

Notes

The authors declare no competing financial interest.

■ ACKNOWLEDGMENTS

This work was supported by the Project of Education Department of Liaoning Province (No. LJKMZ20220959), the National Natural Science Foundation of China (No. 51971106). Science and Technology Innovation Talent Project of Liaoning Provincial Department of Education (LJ222411632049, LJ222411632081).

■ REFERENCES

(1) Reier, T.; Nong, H. N.; Teschner, D.; Schlögl, R.; Strasser, P. Electrocatalytic Oxygen Evolution Reaction in Acidic Environments - Reaction Mechanisms and Catalysts. *Adv. Energy Mater.* **2017**, *7* (1), No. 1601275.

(2) Ansari, M. S.; Kim, H. Enhanced Electrocatalytic Oxygen Evolution Reaction Kinetics Using Dual-Phase Engineering of Self-Supported Hierarchical NiCoV $(OH)_x$ Nanowire Arrays. *Fuel* **2021**, *304*, No. 121309.

(3) Xu, S. L.; Zhao, R. D.; Li, R. Y.; Li, J.; Xiang, J.; Guo, F. Y.; Wu, F. F.; et al. Constructing High-Performance Supercapacitors and Electrochemical Water Splitting Electrode Materials through Core−Shell Structured Co_9S_8@$Ni(OH)_2$ Nanosheets. *J. Mater. Chem. A* **2024**, *12*, 15950−15965.

(4) Liu, X. Y.; Zhang, W. C.; Wu, X.; Cho, Y.-R. Porous Fe-Doped Ni_3P/CoP_3 Isomerism as a Highly Durable Electrocatalyst for Hydrogen Generation. *Energy Mater. Adv.* **2025**, *6*, No. 160.

(5) Bo, S.; Wang, T.; Lv, T.; Wu, H.; Feng, Z.; Miao, L.; Meng, C.; et al. Rapid Synthesis of Boron-MWW Zeolite through a Solvent-Free Strategy. *Chem. Res. Chin. Univ.* **2024**, *40*, 1245−1255.

(6) Jin, H.; Joo, J.; Chaudhari, N. K.; Choi, S. I.; Lee, K. Recent Progress in Bifunctional Electrocatalysts for Overall Water Splitting under Acidic Conditions. *Chem. Electro. Chem.* **2019**, *6*, 3244−3253.

(7) Li, R. Y.; Xu, S. L.; Ai, Z. Q.; Qi, J. G.; Wu, F. F.; Zhao, R. D.; Zhao, D. P. Interface Engineering Accelerated Surface Reconstruction for Electrocatalytic Water Splitting and Energy Storage Device through Hybrid Structured $ZnCo_2O_4$@NiCo-LDH Nanocomposite. *Int. J. Hydrogen Energy* **2024**, *91*, 867−876.

(8) Wang, M. D.; Liu, X. Y.; Wu, X. Realizing Efficient Electrochemical Overall Water Electrolysis through Hierarchical CoP@NiCo-LDH Nanohybrids. *Nano Energy* **2023**, *114*, No. 108681.

(9) He, K.; Tsega, T. T.; Liu, X.; Zai, J. T.; Li, X. H.; Liu, X. J.; Li, W. H.; Ali, N.; Qian, X. F. Utilizing the Space-Charge Region of the FeNi-LDH/CoP p−n Junction to Promote Performance in Oxygen Evolution Electrocatalysis. *Angew. Chem., Int. Ed.* **2019**, *58*, 11903−11909.

(10) Cao, Y.; Wang, T.; Li, X.; Zhang, L. C.; Luo, Y. L.; Zhang, F.; Asiri, A. M.; Hu, J. M.; Liu, Q.; Sun, X. P. A Hierarchical CuO@NiCo Layered Double Hydroxide Core−Shell Nanoarray as an Efficient Electrocatalyst for the Oxygen Evolution Reaction. *Inorg. Chem. Front.* **2021**, *8*, 3049−3054.

(11) Zhou, H.; Li, R.; Xu, S.; Zhang, B.; Zhao, R.; Zhao, X.; Zhao, D. Interface Engineering Induced Homogeneous Isomeric Bimetallic of CoSe/$NiSe_2$ Electrocatalysts for High Performance Water/Seawater Splitting. *Adv. Sustainable Syst.* **2025**, *9*, No. 2400849.

(12) Sun, T.; Tang, Z. Y.; Zang, W. J.; Li, Z. J.; Li, J.; Li, Z. H.; Cao, L.; Rodriguez, J. S. D.; Mariano, C. M.; Xu, H. M.; Lyu, P.; Hai, X.; Lin, H. H.; Sheng, X. Y.; Shi, J. W.; Zheng, Y.; Lu, Y. R.; He, Q.; Chen, J. S.; Novoselov, K. S.; Chuang, C. H.; Xi, S. B.; Luo, X.; Lu, J. Ferromagnetic Single-Atom Spin Catalyst for Boosting Water Splitting. *Nat. Nanotechnol.* **2023**, *18*, 763−771.

(13) Abdullah, M. I.; Hameed, A.; Hu, T. P.; Zhang, N.; Ma, M. M. Crystalline Multi-Metal Nanosheets Array with Enriched Oxygen Vacancies as Efficient and Stable Bifunctional Electrocatalysts for Water Splitting. *ACS Appl. Energy Mater.* **2019**, *2*, 8919−8929.

(14) Jian, J.; Yuan, L.; Qi, H.; Sun, X.; Zhang, L.; Li, H.; Feng, S. Sn−Ni_3S_2 Ultrathin Nanosheets as Efficient Bifunctional Water-Splitting Catalysts with a Large Current Density and Low Overpotential. *J. Mater. Chem. A* **2018**, *6*, 13901−13907.

(15) Zhang, S. S.; Li, R. Y.; Li, X.; Tian, Y. Q.; Zhao, R. D.; Xiang, J.; Wu, F. f.; Zhao, D. P. Hydrothermally Synthesized $NiSe_2$ Nanospheres for Efficient Bifunctional Electrocatalysis in Alkaline Seawater Electrolysis: High Performance and Stability in HER and OER. *Mater. Res. Bull.* **2025**, *189*, No. 113463.

(16) Lv, J.; Liu, P.; Yang, F.; Xing, L.; Wang, D.; Chen, X.; Wang, G.; et al. 3D Hydrangea macrophylla-Like Nickel−Vanadium Metal−Organic Frameworks Formed by Self-Assembly of Ultrathin 2D Nanosheets for Overall Water Splitting. *ACS Appl. Mater. Interfaces.* **2020**, *12*, 48495−48510.

(17) Zander, J.; Marschall, R. 1 min Synthesis of Phase Pure Nanocrystalline High-Entropy Sulfides for Efficient Water Electrolysis. *EcoEnergy* **2025**, *3* (2), 482−498.

(18) Cao, H.; Li, Z.; Xie, Y.; Xiao, F.; Wang, H.; Wang, X.; Pan, K.; Cabot, A. Hierarchical CoP Nanostructures on Nickel Foam as Efficient Bifunctional Catalysts for Water Splitting. *ChemSusChem* **2021**, *14*, 1094−1102.

(19) He, K.; Tsega, T. T.; Liu, X.; Zai, J.; Li, X. H.; Liu, X.; et al. Utilizing the Space-Charge Region of the FeNi-LDH/CoP p−n Junction to Promote Performance in Oxygen Evolution Electrocatalysis. *Angew. Chem., Int. Ed.* **2019**, *58*, 11903−11909.

(20) Zhang, B. Y.; Xu, S. L.; Li, J.; Zhou, H. Y.; Li, X.; Zhao, R. D.; Wu, F. f.; Zhao, D. Excellent Electrocatalytic Performance of $CuCo_2S_4$ Nanowires for High-Efficiency Overall Water Splitting in Alkaline and Seawater Media. *CrystEngComm* **2025**, *27*, 3700−3711.

(21) Sher Shah, M. S. A.; Jang, G. Y.; Zhang, K.; Park, J. H. Transition Metal Carbide-Based Nanostructures for Electrochemical Hydrogen and Oxygen Evolution Reactions. *EcoEnergy* **2023**, *1*, 344−374.

(22) Gao, Z.-W.; Liu, J.-Y.; Chen, X.-M.; Zheng, X.-L.; Mao, J.; Liu, H.; Ma, T.; Li, L.; Wang, W.-C.; Du, X.-W. Engineering NiO/NiFe LDH Intersection to Bypass Scaling Relationship for Oxygen Evolution Reaction via Dynamic Tridimensional Adsorption of Intermediates. *Adv. Mater.* **2019**, *31*, No. 1804769.

(23) Zhang, Z.; Liu, Y.; Su, X.; Zhao, Z.; Mo, Z.; Wang, C.; Gao, S.; et al. Electro-Triggered Joule Heating Method to Synthesize Single-Phase CuNi Nano-Alloy Catalyst for Efficient Electrocatalytic Nitrate Reduction toward Ammonia. *Nano Res.* **2023**, *16*, 6632−6641.

(24) Liu, Y.; Zhou, L.; Liu, S.; Li, S.; Zhou, J.; Li, X.; Chen, X.; Sun, K.; Li, B.; Jiang, J.; Pang, H. Fe, N-Inducing Interfacial Electron Redistribution in NiCo Spinel on Biomass-Derived Carbon for Bifunctional Oxygen Conversion. *Angew. Chem., Int. Ed.* **2024**, No. e202319983.

(25) Zhao, W.; Xu, H.; Luan, H.; Chen, N.; Gong, P.; Yao, K.; Shen, Y.; Shao, Y. NiFe Layered Double Hydroxides Grown on a Corrosion-Cell Cathode for Oxygen Evolution Electrocatalysis. *Adv. Energy Mater.* **2021**, *12*, No. 2102372.

(26) Pan, Y.; Zhao, F.; Ji, G.; Xu, S.; Li, R.; Zhou, H.; Wu, F.; et al. Electrocatalytic Performance of Ni-Based High-Entropy Alloys with Unique Structural Features in Alkaline and Seawater Electrolysis under − 10°C. *Int. J. Hydrogen Energy* **2025**, *127*, 147−159.

(27) Jung, S. Y.; Kim, H. M.; Hwang, S.; Jeung, D. G.; Rhee, K. J.; Oh, J. M. Physicochemical Properties and Hematocompatibility of Layered Double Hydroxide-Based Anticancer Drug Methotrexate Delivery System. *Pharmaceutics* **2020**, *12* (12), No. 1210.

(28) Zhang, Y.; Qian, J.; Wang, P.; He, Y.; Lu, B.; Tang, S.; Xu, K. Rapid Degradation of Levofloxacin Using Peroxymonosulfate Activated by $SrTiO_3/CoFe_2O_4$/rGO Magnetic Nano-Composite: Efficiency, Stability, and Mechanism Investigation. *Sep. Purif. Technol.* **2023**, *309*, No. 123075.

(29) Lu, Z.; Qian, L.; Tian, Y.; Li, Y.; Sun, X.; Duan, X. Ternary NiFeMn Layered Double Hydroxides as Highly-Efficient Oxygen Evolution Catalysts. *Chem. Commun.* **2016**, *52* (5), 908−911.

https://doi.org/10.1021/acs.cgd.5c01006
Cryst. Growth Des. XXXX, XXX, XXX−XXX

(30) Wang, B.; Jiao, S.; Wang, Z.; Lu, M.; Chen, D.; Kang, Y.; Pang, G.; Feng, S. Rational Design of NiFe LDH@Ni_3N Nano/Microsheet Arrays as a Bifunctional Electrocatalyst for Overall Water Splitting. *J. Mater. Chem. A* **2020**, *8*, 17202−17211.
(31) Yan, Y.; Ge, X.; Liu, Z.; Wang, J. Y.; Lee, J. M.; Wang, X. Facile Synthesis of Low-Crystalline MoS_2 Nanosheet-Coated CNTs for Enhanced Hydrogen Evolution Reaction. *Nanoscale* **2013**, *5* (17), 7768−7771.
(32) Stephenson, T.; Li, Z.; Olsen, B.; Mitlin, D. Lithium Ion Battery Applications of Molybdenum Disulfide (MoS_2) Nanocomposites. *Energy Environ. Sci.* **2014**, *7* (1), 209−231.
(33) Lin, J.; Wang, P.; Wang, H.; Li, C.; Si, X.; Qi, J.; Feng, J.; et al. Defect-Rich Heterogeneous MoS_2/NiS_2 Nanosheets Electrocatalysts for Efficient Overall Water Splitting. *Adv. Sci.* **2019**, *6*, No. 1900246.
(34) Liu, Y.; Jiang, S.; Li, S.; Zhou, L.; Li, Z.; Li, J.; Shao, M. Interface Engineering of (Ni, Fe) S_2@MoS_2 Heterostructures for Synergetic Electrocatalytic Water Splitting. *Appl. Catal., B* **2019**, *247*, 107−114.
(35) Wong, K. C.; Lu, X.; Cotter, J.; Eadie, D. T.; Wong, P. C.; Mitchell, K. A. R. Surface and Friction Characterization of MoS_2 and WS_2 Third Body Thin Films under Simulated Wheel/Rail Rolling−Sliding Contact. *Wear* **2008**, *264* (7−8), 526−534.
(36) Zhang, B.; Ji, Y.; Wang, S.; Zhang, P.; Zhang, S.; Zhou, P.; Wu, J.; Miao, S. MoS_2 Nanoparticles Anchored on Exfoliated NiFe-LDH Nanosheets via Electrodeposition as Multifunctional Electrodes for Energy Conversion and Storage Applications. *J. Power Sources.* **2025**, *657*, No. 238120.
(37) Cao, N.; Di, Y.; Chen, S.; Jin, X.; Liu, M.; Shao, Q.; Zang, X. Hierarchical Nanoarchitecture with NiFe-LDH on MoS_2 for Enhanced Electrocatalysis of Hydrogen Evolution in Alkaline Media. *Electrochim. Acta* **2023**, *467*, No. 143079.
(38) Wen, H. Z.; Zhao, Y.; Zhang, H. T.; Wan-Me, Z. X.; Wan, X. Y.; Xie, Y. L. Construction of an Advanced MoS_2/MoO_3/NiFe-LDH/NF Heterostructure Catalyst toward Boosting Efficient Alkaline Oxygen Evolution Reaction. *Catal. Sci. Technol.* **2025**, *15*, 3871−3877.
(39) Luo, Y.; Duan, Y.; Xie, Y.; Wang, Y.; Li, X.; Liu, Y.; Xu, S. Promotion of the Oxygen Evolution Reaction by Introducing MoS_2 into CoFe LDH via Improved Charge Transfer and Electrocatalytical Activity. *Fuel* **2024**, *371*, No. 131993.
(40) Li, C.; Yang, T.; Fan, J.; Liu, E.; Zhao, B.; Sun, T. NiFe LDH/MoS_2/Ni_3S_2 pn/Mott−Schottky Heterojunction for Efficient Hydrogen Generation Coupled with Electrochemical Oxidation of Organic Molecules. *J. Alloys Compd.* **2024**, *970*, No. 172710.
(41) Cai, J.; Liu, H.; Luo, Y.; Xiong, Y.; Zhang, L.; Wang, S.; Xiao, K.; Liu, Z. Q. Single-Phase Bimetal Sulfide or Metal Sulfide Heterojunction: Which One is Better for Reversible Oxygen Electrocatalyst? *J. Energy Chem.* **2022**, *74*, 420−428.
(42) Chen, Y.; Yao, H.; Kong, F.; Tian, H.; Meng, G.; Wang, S.; Shi, J.; et al. V_2C MXene Synergistically Coupling FeNi LDH Nanosheets for Boosting Oxygen Evolution Reaction. *Appl. Catal., B* **2021**, *297*, No. 120474.
(43) Kitiphatpiboon, N.; Chen, M.; Feng, C.; Zhou, Y.; Liu, C.; Feng, Z.; Guan, G.; et al. Modification of Spinel $MnCo_2O_4$ Nanowire with NiFe-Layered Double Hydroxide Nanoflakes for Stable Seawater Oxidation. *J. Colloid Interface Sci.* **2023**, *632*, 54−64.
(44) Cao, N.; Di, Y.; Chen, S.; Jin, X.; Liu, M.; Shao, Q.; Zang, X. Hierarchical Nanoarchitecture with NiFe-LDH on MoS_2 for Enhanced Electrocatalysis of Hydrogen Evolution in Alkaline Media. *Electrochim. Acta* **2023**, *467*, No. 143079.
(45) Yu, L.; Wu, L.; McElhenny, B.; Song, S.; Luo, D.; Zhang, F.; Ren, Z.; et al. Ultrafast Room-Temperature Synthesis of Porous S-Doped Ni/Fe (Oxy)hydroxide Electrodes for Oxygen Evolution Catalysis in Seawater Splitting. *Energy Environ. Sci.* **2020**, *13*, 3439−3446.
(46) Cui, B.; Hu, Z.; Liu, C.; Liu, S.; Chen, F.; Hu, S.; Hu, W.; et al. Heterogeneous Lamellar-Edged Fe-Ni$(OH)_2/Ni_3S_2$ Nanoarray for Efficient and Stable Seawater Oxidation. *Nano Res.* **2021**, *14*, 1149−1155.
(47) Wu, Z.; Li, L.; Liao, T.; Chen, X.; Jiang, W.; Luo, W.; Sun, Z. Janus Nanoarchitectures: From Structural Design to Catalytic Applications. *Nano Today.* **2018**, *22*, 62−82.
(48) Teng, W.; Sun, Z.; Xie, J.; Wang, Z.; Zheng, X.; Tang, B. In-Situ Formation of Amorphous Co−Al−P Layer on CoAl Layered Double Hydroxide Nanoarray as Neutral Electrocatalysts for Hydrogen Evolution Reaction. *Front. Chem.* **2020**, *8*, No. 552795.
(49) Yang, Y.; Zhang, K.; Lin, H.; Li, X.; Chan, H. C.; Yang, L.; Gao, Q. MoS_2-Ni_3S_2 Heteronanorods as Efficient and Stable Bifunctional Electrocatalysts for Overall Water Splitting. *ACS Catal.* **2017**, *7*, 2357−2366.
(50) Guo, L.; Chi, J.; Cui, T.; Zhu, J.; Xia, Y.; Guo, H.; Lai, J.; Wang, L. Phosphorus Defect Mediated Electron Redistribution to Boost Anion Exchange Membrane-Based Alkaline Seawater Electrolysis. *Adv. Energy Mater.* **2024**, *14*, No. 2400975.
(51) Shit, S.; Ghosh, S.; Bolar, S.; Murmu, N. C.; Kuila, T. Understanding the Synergistic Effect in Oxygen Evolution Reaction Catalysis from Chemical Kinetics Point of View: An Iron Oxide/Nickel Oxide Case Study. *J. Electrochem. Soc.* **2020**, *167*, No. 116514.
(52) Plank, C.; Rüther, T.; Jahn, L.; Schamel, M.; Schmidt, J. P.; Ciucci, F.; Danzer, M. A. A Review on the Distribution of Relaxation Times Analysis: A Powerful Tool for Process Identification of Electrochemical Systems. *J. Power Sources* **2024**, *594*, No. 233845.
(53) Maradesa, A.; Py, B.; Huang, J.; Lu, Y.; Iurilli, P.; Mrozinski, A.; Ciucci, F.; et al. Advancing Electrochemical Impedance Analysis through Innovations in the Distribution of Relaxation Times Method. *Joule* **2024**, *8*, 1958−1981.
(54) Ao, F.; Ma, J.; Li, H.; Meng, T.; Zhu, Y.; Huang, K.; Wang, P.; Zhao, Y. Iron-Doped Carbon Supported Nickel Selenide Heterogeneous Materials for Dual-Function Water Electrolysis Catalysts. *Appl. Surf. Sci.* **2024**, *664*, No. 160233.
(55) He, L.; Wang, N.; Sun, B.; Zhong, L.; Yao, M.; Hu, W.; Komarneni, S. High-Entropy FeCoNiMn (oxy)hydroxide as High-Performance Electrocatalyst for OER and Boosting Clean Carrier Production under Quasi-Industrial Conditions. *J. Cleaner Prod.* **2022**, *356*, No. 131680.
(56) Song, Q.; Li, K.; Cao, Z.; Mi, Y.; Kong, Q.; He, G.; Zhang, X.; et al. Doping La into NiFe LDH/NiS Heterostructure Achieving High-Current-Density Oxygen Evolution for Anion Exchange Membrane Water Electrolysis. *Chem. Eng. J.* **2025**, *504*, No. 157526.
(57) Liu, T.; Yu, X.; Yu, S.; Yang, H.; Sun, Q.; Wang, C.; Li, S.; Zheng, J. Y. Robust CoP@NiFe LDH/Ni Heterostructured Electrodes for Efficient Overall Water Splitting with High Current Density. *J. Alloys Compd.* **2024**, *973*, No. 172886.
(58) Feng, Y. Y.; Deng, G.; Wang, X. Y.; Zhu, M.; Bian, Q. N.; Guo, B. S. $MoS_2/NiFeS_2$ Heterostructure as a Highly Efficient Electrocatalyst for Overall Water Splitting at High Current Densities. *Int. J. Hydrogen Energy* **2023**, *48*, 12354−12363.
(59) Fu, X.; Liao, H.; Zhang, Z.; Zheng, Y.; Lu, J.; Cheng, S.; Jiang, Y.; Gao, Y. Medium-Entropy Heterostructure of Crystalline NiCoFeP@Amorphous NiCoFe-LDH for Industrial-Current Density and Ultrastable Overall Water Splitting. *Chem. Eng. J.* **2025**, *505*, No. 159520.
(60) Ferreira de Araújo, J.; Dionigi, F.; Merzdorf, T.; Oh, H. S.; Strasser, P. Evidence of Mars−Van−Krevelen Mechanism in the Electrochemical Oxygen Evolution on Ni-Based Catalysts. *Angew. Chem., Int. Ed.* **2021**, *60*, 14981−14988.
(61) Zhou, S.; Wang, J.; Li, J.; Fan, L.; Liu, Z.; Shi, J.; Cai, W. Surface-Growing Organophosphorus Layer on Layered Double Hydroxides Enables Boosted and Durable Electrochemical Freshwater/Seawater Oxidation. *Appl. Catal., B* **2023**, *332*, No. 122749.
(62) Yu, L.; Wu, L.; McElhenny, B.; Song, S.; Luo, D.; Zhang, F.; Yu, Y.; Chen, S.; Ren, Z. Ultrafast Room-Temperature Synthesis of Porous S-Doped Ni/Fe (oxy)hydroxide Electrodes for Oxygen Evolution Catalysis in Seawater Splitting. *Energy Environ. Sci.* **2020**, *13*, 3439−3446.
(63) Jin, H.; Wang, J.; Su, D.; Wei, Z.; Pang, Z.; Wang, Y. In Situ Cobalt−Cobalt Oxide/N-Doped Carbon Hybrids as Superior Bifunctional Electrocatalysts for Hydrogen and Oxygen Evolution. *Am. Chem. Soc.* **2015**, *137*, 2688−2694.
(64) Gaur, A. P.; Zhang, B.; Lui, Y. H.; Tang, X.; Hu, S. Morphologically Tailored Nano-Structured MoS_2 Catalysts via

https://doi.org/10.1021/acs.cgd.5c01006
Cryst. Growth Des. XXXX, XXX, XXX−XXX

Introduction of Ni and Co Ions for Enhanced HER Activity. *Appl. Surf. Sci.* **2020**, *516*, No. 146094.
(65) Yan, W.; Zhao, Z.; Xin, Z.; Hu, J.; Xia, J.; Zhou, L.; Sun, Y.; et al. Atomic-Scale Robust Modulation of Pt on Monolayer MoS_2 for Enhanced on-Chip Hydrogen Evolution Reaction. *Adv. Funct. Mater.* **2025**, *35*, No. 2423262.
(66) Gong, Z.; Cheng, W.; Fang, Z.; Li, N.; Qin, Y.; Wang, X.; Bao, H. Interface Engineering Induced NiFe/Ni-Mo-S@CC Heterostructure with Excellent OER and HER Performance. *Ionics* **2023**, *29*, 4787−4796.
(67) Choi, J.; Nkhama, A.; Kumar, A.; Mishra, S. R.; Perez, F.; Gupta, R. K. A Facile Preparation of Sulfur Doped Nickel−Iron Nanostructures with Improved HER and Supercapacitor Performance. *Int. Hydrogen Energy* **2022**, *47*, 7511−7521.
(68) Martirez, J. M. P.; Carter, E. A. Unraveling Oxygen Evolution on Iron-Doped β-Nickel Oxyhydroxide: The Key Role of Highly Active Molecular-Like Sites. *Am. Chem. Soc.* **2019**, *141*, 693−705.
(69) Michael, J. D.; Demeter, E. L.; Illes, S. M.; Fan, Q.; Boes, J. R.; Kitchin, J. R. Alkaline Electrolyte and Fe Impurity Effects on the Performance and Active-Phase Structure of NiOOH Thin Films for OER Catalysis Applications. *Phys. Chem. C* **2015**, *119*, 11475−11481.
(70) Kim, B. J.; Piao, G.; Kim, S.; Yang, S. Y.; Park, Y.; Han, D. S.; Park, H.; et al. High-Efficiency Solar Desalination Accompanying Electrocatalytic Conversions of Desalted Chloride and Captured Carbon Dioxide. *ACS Sustainable Chem. Eng.* **2019**, *7*, 15320−15328.
(71) Jia, T.; Wu, J.; Xiao, Y.; Liu, Q.; Wu, Q.; Qi, Y.; Qi, X. Self-Grown Oxygen Vacancies-Rich CeO_2/BiOBr Z-Scheme Heterojunction Decorated with rGO as Charge Transfer Channel for Enhanced Photocatalytic Oxidation of Elemental Mercury. *J. Colloid Interface Sci.* **2021**, *587*, 402−416.
(72) Shao, B.; Liu, X.; Liu, Z.; Zeng, G.; Liang, Q.; Liang, C.; Gong, S.; et al. A Novel Double Z-Scheme Photocatalyst $Ag_3PO_4/Bi_2S_3/Bi_2O_3$ with Enhanced Visible-Light Photocatalytic Performance for Antibiotic Degradation. *Chem. Eng. J.* **2019**, *368*, 730−745.

https://doi.org/10.1021/acs.cgd.5c01006
Cryst. Growth Des. XXXX, XXX, XXX−XXX